Consistent Large Eddy Simulation of a temporal mixing layer laden with evaporating drops. Part I: Direct Numerical Simulation and Formulation

By NORA A. OKONG'O and JOSETTE BELLAN †

Jet Propulsion Laboratory, California Institute of Technology, Pasadena, CA 91109-8099, USA

(Received 18 July 2002)

Direct Numerical Simulation (DNS) is conducted of a three-dimensional temporal mixing layer whose lower stream is initially laden with liquid drops which may evaporate during the simulation. The gas-phase equations are written in an Eulerian frame for two perfect gas species (carrier gas and vapor emanating from the drops), while the liquid-phase equations are written in a Lagrangian frame. The effect of drop evaporation on the gas phase is considered through mass, momentum and energy source terms. Simulations are performed for layers with different initial Reynolds numbers and initial liquid-mass loadings, each layer evolving to attain a transitional state. The Large Eddy Simulation (LES) equations that would govern the evolution of a spatially filtered flow field are derived and the magnitude of the terms in the LES equations are computed at the transitional states. Budgets of these equations show that for the mass loadings considered, the filtered source terms are smaller than the resolved inviscid terms and some subgrid scale (SGS) terms, but larger than the resolved viscous stresses and the heat and mass fluxes. Based on the budgets, the LES equations are simplified to contain resolved terms

† Author for correspondence: Josette.Bellan@jpl.nasa.gov

and two types of unresolved terms (SGS fluxes and filtered source terms). A parallel perspective on the importance of the source terms is obtained by deriving the irreversible entropy production (i.e. the entropy dissipation) equation for a two-phase flow with phase change, and by evaluating the contributions to this equation at transition. In addition to source-term contributions, the dissipation contains contributions due to viscous stresses, heat fluxes and species mass fluxes. For both the DNS and LES flow fields, the two leading terms are the dissipation due to the energy source term (producing dissipation at the large scales, but removing dissipation at the small scales), and the dissipation due to the chemical potential of the mass source (removing dissipation at the large scales, but producing dissipation at the small scales). The dissipation related to the viscous stresses is only third in magnitude. Therefore, it is clear that effort should be devoted to the accurate modeling of both the SGS fluxes and the filtered source terms in the LES equations.

---

1. Introduction

The accurate modeling of two-phase (TP) turbulent flows has been a long standing problem that is so far unresolved. Situations that could benefit from such models occur in a wide range of disciplines encompassing atmospheric turbulence (e.g. tornadoes and sand storms), oceanography (e.g. motion of schools of fish), and devices based on spray operation (e.g. household cleaning products, pharmaceutical inhalers, office printers, gas turbine engines, spray-chemical-conversion reactors). In all these situations, the interaction of the phases through momentum, energy and sometimes mass transfer, determines the character of the flow. Because this interaction occurs at scales that are much smaller than the scale of practical interest, it is clear that routine simulations of such flows can-

not embed a resolution of the physics at the interaction scales, indicating that phase interactions must be modeled instead.

For TP flows with particles that are much smaller than the Kolmogorov scale and which have a volumetrically small loading ($\simeq 10^{-3}$), Boivin *et al.* (1998) have shown that the particles can be treated as point sources of momentum from the gas-phase perspective. The same derivation applies to show that evaporating drops under the same size and loading conditions can be treated as point sources of mass, momentum and energy for the gas. Although the volumetric loading is small, the mass loadings can be considerably larger ($\gtrsim 10^{-1}$) due to the density ratio between the liquid and carrier gas being $O\left(10^3\right)$, and therefore the drops may considerably influence the flow. The interaction between drops and gas flow involves both the effect of the flow field on the drops (as the drop far-field), and of the drops on the flow field (as gas-phase mass, momentum and energy sources) i.e. two-way coupling. In considering the resolution necessary for Direct Numerical Simulations (DNS) of TP flows, we recall that for DNS of single-phase (SP) turbulent flows, no turbulence model is used, and therefore the appropriate flow resolution is determined by the Kolmogorov scale. By treating the drops as point sources for the gas, essentially the same resolution can be used for TP flows. Then TP flow DNS entails simulating the gas phase in an Eulerian frame, at the SP resolution, and tracking all the individual drops, which are treated as point sources, in a Lagrangian frame. Recent studies using this DNS methodology, for isotropic turbulence, include those of Boivin *et al.* (1998) and Mashayek & Jaberi (1999) for solid particles without phase change and those of Mashayek (1998*a*) and Réveillon & Vervisch (2000) for evaporating drops. Other DNS with evaporating drops have been performed by Mashayek (1998*b*) for homogeneous shear flow and by Miller & Bellan (1999) and Miller & Bellan (2000) for temporal mixing layers.

Unfortunately, DNS has high resolution requirements that presently limit it to relatively low Reynolds number turbulent flows in geometrically simple domains. Large Eddy Simulation (LES) is a promising alternative to DNS. The essence of the LES methodology is to spatially filter the flow, and then simulate the filtered (large-scale) flow field, while modeling the subgrid-scale (SGS) unresolved flow field. Specifically, the LES gas-phase equations are derived by filtering the DNS gas-phase equations, leading to unclosed terms, which for SP flow are primarily the SGS fluxes that arise from the convective terms. (The SGS fluxes appearing in the momentum equation are usually called SGS stresses.) Since only the large scales need to be resolved, LES may be conducted with reduced flow field resolution compared to DNS. Consistent LES then means tracking a reduced number of 'computational' drops to represent the physical drops. In this context, TP LES has additional modeling requirements compared to SP LES; whereas DNS requires modeling the interaction between individual drops and the unfiltered flow field, in LES neither the individual drops nor the unfiltered flow field are available and their interaction must be modeled from that between the filtered flow field and the computational drops.

Recent LES of TP flows include those by Boivin *et al.* (2000), Deutsch & Simonin (1991), Simonin *et al.* (1993), Uijttewaal & Oliemans (1996), Wang & Squires (1996) and Yamamoto *et al.* (2001). These LES all considered an incompressible gas phase laden with small solid particles, with the particles not affecting the evolution of the gas phase i.e. one-way coupling, and used actual or 'computational' particles whose evolution was entirely governed by the resolved flow field. When Wang & Squires (1996) included SGS effects by modifying the gas-phase velocity felt by the particles, they found them to be negligible. The LES of Boivin *et al.* (2000) and Yamamoto *et al.* (2001) also included two-way coupling, but still neglected SGS effects on the particles. The SGS modeling requirement in these studies was confined to the gas phase, facilitating the use of the

large body of work on SGS flux models for incompressible SP flow. Much less research has been devoted to compressible-flow SGS flux modeling and has mostly been confined to the energy equation in single-species SP flows (e.g. Erlebacher *et al.* (1992), Fureby (1996), Martin *et al.* (2000)). SGS TP flow models that treated the drop contribution but did not reduce the size of the drop ensemble or consider the effect of the drops on the flow field were presented by Miller & Bellan (2000) and Okong'o & Bellan (2000).

In the present study, we seek to develop a consistent LES formulation for TP flows with evaporating drops, along with the necessary models for the unresolved quantities. To this end, we perform DNS to create a database upon which prospective models will be tested *a priori*. The DNS undertaken in this study generally follows the approach of Miller & Bellan (1999) and Miller & Bellan (2000). However, similar to Réveillon & Vervisch (2000) and unlike Mashayek (1998*a*) and Mashayek (1998*b*), we also include the effect of the species diffusional fluxes in the heat flux; this effect is important at the low temperature difference between gas and drops (compared to those typical of combustion problems) specified in the present DNS in order to foster interaction between drops and flow field.

This paper is organized as follows: In § 2 we present the DNS formulation. This formulation consists of a set of coupled conservation equations for the gas phase and the liquid phase (i.e. the drops). The coupling describing the interaction between the two phases is provided in the gas-phase conservation equations by source terms. In § 3 we analyze the DNS results; in particular we evaluate the form of the heat and mass fluxes. The gas-phase LES equations are developed in § 4 and assumptions that may simplify these equations are examined using the DNS database. Thereafter, the contribution of the source terms is examined by considering the budget of the LES equations. The final form of the LES equations are then presented, in which only the SGS fluxes and the

filtered source terms need to be modeled. A parallel perspective on the importance of the source terms is presented in § 5, wherein the irreversible entropy production (i.e. the entropy dissipation) equation for two-phase flow with phase change is derived and evaluated for transitional DNS and LES flow fields. The unclosed quantities in the final LES equations will be modeled, *a priori*, in Part II of this investigation, leading to a modeling approach that will be validated, in Part III, by means of an *a posteriori* study. Finally, the paper is summarized in § 6 with conclusions for the *a priori* study to be undertaken in Part II.

2. DNS equations

The gas phase equations are formulated in an Eulerian frame for two calorically perfect species, namely the carrier gas and the vapor evolving from the drops. Each drop, tracked in a Lagrangian frame, is assumed to be spherical, and, consistent with the drop description as a point source, its internal temperature and density are assumed uniform. Furthermore, we neglect unsteady drag and added mass effects, as well as Basset history forces, all of which are small for liquid-to-gas density ratios (Boivin *et al.* (1998)). Drop collisions are assumed negligible.

2.1. *Gas-phase equations*

For ease of notation, we define the vector of gas-phase conservative variables $\phi = \{\rho,\ \rho u_i,\ \rho e_t,\ \rho Y_V\}$ and denote the flow field as ϕ, where ρ is the density, u_i is the velocity in the x_i coordinate direction, e_t is the total energy and Y_V is the vapor (subscript V) mass fraction (the carrier gas, subscript C, mass fraction is Y_C; $Y_C + Y_V = 1$). The gas-phase conservation equations are:

$$\frac{\partial \rho}{\partial t} + \frac{\partial (\rho u_j)}{\partial x_j} = S_I, \tag{2.1}$$

$$\frac{\partial(\rho u_i)}{\partial t}+\frac{\partial(\rho u_i u_j)}{\partial x_j}=-\frac{\partial p}{\partial x_i}+\frac{\partial \sigma_{ij}}{\partial x_j}+S_{II,i}, \tag{2.2}$$

$$\frac{\partial(\rho e_t)}{\partial t}+\frac{\partial(\rho e_t u_j)}{\partial x_j}=-\frac{\partial(p u_j)}{\partial x_j}-\frac{\partial q_j}{\partial x_j}+\frac{\partial(\sigma_{ij}u_i)}{\partial x_j}+S_{III}, \tag{2.3}$$

$$\frac{\partial(\rho Y_V)}{\partial t}+\frac{\partial(\rho Y_V u_j)}{\partial x_j}=-\frac{\partial j_{Vj}}{\partial x_j}+S_I, \tag{2.4}$$

$$\frac{\partial(\rho Y_C)}{\partial t}+\frac{\partial(\rho Y_C u_j)}{\partial x_j}=-\frac{\partial j_{Cj}}{\partial x_j}, \tag{2.5}$$

where S_I, $S_{II,i}$ and S_{III} are source terms due to the action of the drops. The thermodynamic variables to be computed from ϕ are the internal energy ($e = e_t - e_k$, where the kinetic energy is $e_k = u_i u_i/2$), the pressure (p), the temperature (T) and the enthalpy ($h = e + p/\rho$). We assume perfect gases, for which

$$p(\phi)=\rho R(\phi)\,T(\phi), \tag{2.6}$$

where $R = Y_V R_V + Y_C R_C$, $R_V = R_u/m_V$, $R_C = R_u/m_C$, R_u is the universal gas constant and m_C and m_V are the molar weights of the carrier gas and vapor respectively, and

$$h(\phi)=h_V Y_V + h_C Y_C, \tag{2.7}$$

where h_C and h_V are the enthalpies of the pure gases

$$h_C=\int C_{p,C}(T)\,dT, \quad h_V=\int C_{p,V}(T)\,dT, \tag{2.8}$$

which are calculated from a given functional form of the heat capacities at constant pressure, $C_{p,C}$ and $C_{p,V}$. For the small temperature and pressure range to be simulated, we assume the gas to be calorically perfect, which means that $C_{p,C}$ and $C_{p,V}$ are constant; then

$$h_C(\phi)=C_{p,C}T, \qquad h_V(\phi)=C_{p,V}T+h_V^0, \tag{2.9}$$

where $C_{p,C} = C_{p,C}(T^0)$, $C_{p,V} = C_{p,V}(T^0)$ and h_V^0 is the reference vapor enthalpy at (T^0, p^0) obtained from integration or tables, which accounts for the enthalpy difference between the vapor and carrier gas at the reference conditions. Then (2.7) can be written

as

$$h(\phi) = C_p(\phi)\,T(\phi) + h_V^0 Y_V, \tag{2.10}$$

where the mixture heat capacity at constant pressure is $C_p = C_{p,V}Y_V + C_{p,C}Y_C$. The temperature T is computed from the internal energy through

$$e(\phi) = C_v(\phi)\,T(\phi) + h_V^0 Y_V, \tag{2.11}$$

where C_v is the mixture heat capacity at constant temperature ($C_v = C_p - R$).

For (2.1)–(2.5), we also specify the following functions of the flow field: the viscous stress,

$$\sigma_{ij}(\phi) = 2\mu\left(S_{ij} - \frac{1}{3}S_{kk}\delta_{ij}\right), \tag{2.12}$$

where μ is the viscosity and

$$S_{ij}(\phi) = \frac{1}{2}\left(\frac{\partial u_i}{\partial x_j} + \frac{\partial u_j}{\partial x_i}\right) \tag{2.13}$$

is the rate of strain; the vapor mass flux,

$$j_{Vj}(\phi) = \rho Y_V V_{Vj}(\phi) = -\rho Y_V\left[\frac{D}{Y_V}\frac{\partial Y_V}{\partial x_j} + Y_C\left(Y_V + Y_C\frac{m_V}{m_C}\right)\left[\frac{m_C}{m_V} - 1\right]\frac{D}{p(\phi)}\frac{\partial p(\phi)}{\partial x_j}\right], \tag{2.14}$$

where thermal diffusion effects have been neglected, V_{Vj} is the vapor diffusion velocity, and D is the diffusion coefficient; the carrier gas mass flux

$$j_{Cj}(\phi) = \rho Y_V V_{Cj}(\phi) = -j_{Vj}; \tag{2.15}$$

and the heat flux,

$$q_j(\phi) = -\lambda\frac{\partial T(\phi)}{\partial x_j} + \left(h_V(\phi) - h_C(\phi)\right)j_{Vj}(\phi), \tag{2.16}$$

where λ is the thermal conductivity. In (2.12), (2.14) and (2.16), μ, D and λ are assumed constant, and may be defined through the Prandtl and Schmidt numbers, $\mathrm{Pr} = \mu C_p/\lambda$ and $Sc = \mu/(\rho D)$. In Miller & Bellan (1999) and Miller & Bellan (2000), the Fick con-

tribution was assumed to dominate the diffusional fluxes, and thus the second (pressure gradient) term was neglected in (2.14); also, the Fourier term was assumed to dominate the heat flux and the second (enthalpy flux) term in (2.16) was not included.

2.2. *Drop (liquid-phase) equations*

The equations describing the drop evolution have been presented in detail by Miller & Bellan (1999) and only their essence is presented here. We define $Z = \{X_i, v_i, T_d, m_d\}$ as the drop field with position X_i, velocity v_i, temperature T_d, and mass m_d. Under the assumptions stated previously, the evolution equations for the drops, in a Lagrangian frame, are:

$$\frac{dX_i}{dt}(Z) = v_i, \tag{2.17}$$

$$\frac{dv_i}{dt}(\psi_f, Z) = \frac{1}{m_d} F_i(\psi_f, Z), \tag{2.18}$$

$$\frac{dT_d}{dt}(\psi_f, \psi_s, Z) = \frac{1}{m_d C_L}\left[Q(\psi_f, Z) + \dot{m}_d(\psi_f, \psi_s, Z) L_V(Z)\right], \tag{2.19}$$

$$\frac{dm_d}{dt}(\psi_f, \psi_s, Z) = \dot{m}_d(\psi_f, \psi_s, Z), \tag{2.20}$$

where F_i is the drag force, Q is the heat flux, $\dot{m}_d$ is the evaporation rate, and C_L is the heat capacity of the drop liquid. L_V is the latent heat of vaporization, which, for calorically perfect gases, is a linear function of temperature, $L_V = h_V^0 - (C_L - C_{p,V})T_d$. The drop evolution depends on the gas-phase primitive variables, $\psi(\phi) = \{u_i, T, Y_V, p\}$, evaluated either at the drop surface (subscript s) or at the drop far-field (subscript f). The far-field variables are taken as the gas-phase primitive variables interpolated to the drop locations. The detailed expressions for F_i, Q, and $\dot{m}_d$ involve validated correlations for point drops which are based on Stokes drag, with particle time constant $\tau_d = \rho_L d^2/(18\mu)$, where ρ_L

is the density of the liquid and d is the drop diameter ($m_d = \rho_L \pi d^3/6$):

$$F_i(\psi_f, Z) = \frac{m_d}{\tau_d} f_1 (u_{i,f} - v_i) \tag{2.21}$$

$$Q(\psi_f, Z) = \frac{m_d}{\tau_d} \frac{Nu}{3\,\mathrm{Pr}} C_{p,f} f_2 (T_f - T_d) \tag{2.22}$$

$$\dot{m}_d(\psi_f, Z) = -\frac{m_d}{\tau_d} \frac{Sh}{3Sc} \ln[1 + B_M] \tag{2.23}$$

In (2.21), f_1 is an empirical correlation to correct the Stokes drag for finite drop Reynolds numbers

$$f_1 = \frac{1 + 0.0545\,\mathrm{Re}_{sl} + 0.1\,\mathrm{Re}_{sl}^{1/2}(1 - 0.03\,\mathrm{Re}_{sl})}{1 + a\,|\mathrm{Re}_b|^b}, \tag{2.24}$$

$$a = 0.09 + 0.077\exp(-0.4\,\mathrm{Re}_{sl}), \qquad b = 0.4 + 0.77\exp(-0.04\,\mathrm{Re}_{sl}), \tag{2.25}$$

based on the slip Reynolds number $\mathrm{Re}_{sl} = |u_{i,f} - v_i|\,\rho d/\mu$ where $u_{i,f} - v_i$ is the slip velocity, and on the blowing Reynolds number $\mathrm{Re}_b = U_b \rho d/\mu$ where U_b is the blowing velocity obtained from the mass conservation relation at the drop surface, $\dot{m}_d = -\pi \rho d^2 U_b$. The correlation of (2.24) is valid for the ranges $0 \leqslant \mathrm{Re}_{sl} \leqslant 100$ and $0 \leqslant \mathrm{Re}_b \leqslant 10$. In (2.22), $C_{p,f} = C_{p,V} Y_{V,f} + C_{p,C} Y_{C,f}$ and $f_2 = \beta/(e^\beta - 1)$, where $\beta = -1.5\,\mathrm{Pr}\,\dot{m}_d \tau_d / m_d$ is constant for drops obeying the classical 'd^2 law' (Williams (1965)). In (2.23), the mass transfer number is $B_M = (Y_{V,s} - Y_{V,f})/(1 - Y_{V,s})$ where the surface vapor mass fraction $Y_{V,s}$ is calculated directly from the mole fraction, $X_{V,s}$, which is obtained by equating the vapor and liquid fugacities at the surface (i.e. $X_{V,s} p_s = p_{sat}$; also $p_s = p_f$), where the saturation pressure, p_{sat}, is provided by the Clausius-Clapeyron relation. This leads to

$$X_{V,s} = \frac{p_{atm}}{p_s} \exp\left[\frac{L_V}{R_V}\left(\frac{1}{T_{B,L}} - \frac{1}{T_d}\right)\right], \qquad Y_{V,s} = \frac{X_{V,s}}{X_{V,s} + (1 - X_{V,s})\, m_C/m_V}, \tag{2.26}$$

where p_{atm}=1 atm and $T_{B,L}$ is the liquid saturation temperature at p_{atm} (i.e. the normal boiling temperature). Finally, the Nusselt, Nu, and Sherwood, Sh, numbers appearing in (2.22) and (2.23) are empirically modified for convective corrections to heat and mass

transfer based on the Ranz-Marshall correlations

$$Nu = 2 + 0.552\ \mathrm{Re}_{sl}^{1/2}\,(\mathrm{Pr})^{1/3}, \qquad Sh = 2 + 0.552\,\mathrm{Re}_{sl}^{1/2}\,(Sc)^{1/3}. \tag{2.27}$$

Except for τ_d, which depends on μ, (2.21)–(2.23) depend essentially on ratios of transport properties through non-dimensional numbers. Therefore, the value of τ_d and thus for a given liquid and drop size, the value of μ determines the interaction time between drops and gas.

2.3. *Source terms*

As in Miller & Bellan (1999), each drop acts as a point source of mass, momentum and energy for the gas phase, with the drop source vector

$$S_d\left(\psi_f, Z\right) = \left\{S_{I,d}, S_{II,i,d}, S_{III,d}\right\}, \tag{2.28}$$

$$S_{I,d} = -\dot{m}_d, \tag{2.29}$$

$$S_{II,i,d} = -\left[F_i + \dot{m}_d v_i\right], \tag{2.30}$$

$$S_{III,d} = -\left[F_i v_i + Q + \dot{m}_d\left(\tfrac{1}{2}v_i v_i + h_{V,s}\right)\right], \tag{2.31}$$

where $h_{V,s} = C_{p,V}T_d + h_V^0$ is the vapor enthalpy at the drop surface. The drop sources in the Lagrangian frame need to be reconstructed in the Eulerian frame to obtain the gas-phase source vector S which contains the terms in (2.1)–(2.4), $S\left(\psi_f, Z\right) = \left\{S_I, S_{II,i}, S_{III}\right\}$. As in Miller & Bellan (1999), we use

$$S\left(\psi_f, Z\right) = \sum_{\alpha} \frac{w_\alpha}{V}\left[S_d\left(\psi_f, Z\right)\right]_\alpha \tag{2.32}$$

where the summation is over all drops α residing within a local numerical discretization volume, V, and the geometrical weighting factor, w_α, is used to distribute the individual drop contributions to the eight nearest neighbor surrounding grid points (i.e. corners of the computational volume V) proportionally to the drop distance from those nodes.

These source terms are then minimally 'smoothed' using a conservative operator so as to retain numerical stability of the Eulerian gas-phase fields.

2.4. *Flow configuration and numerical procedure*

The mixing layer geometric configuration is illustrated in figure 1 where the streamwise (x_1), the cross-stream (x_2), and the spanwise (x_3) coordinates are shown, and the domain lengths are L_1, L_2 and L_3 in each direction. Periodic boundary conditions are used in the x_1 and x_3 directions, and adiabatic slip wall conditions (see Poinsot & Lele (1992)) are employed for the x_2 boundaries. Initially, the gas phase is comprised only of the carrier gas (no vapor). The free-stream velocity $U_0 = M_{c,0}a_{C,0}$ is calculated from a specified value of the convective Mach number $M_{c,0}$ based on the carrier gas initial speed of sound $a_{C,0} = \sqrt{R_C T_{C,0} C_{p,C}/C_{v,C}}$ where $T_{C,0}$ is the initial uniform temperature of the carrier gas at the initial uniform pressure. The initial vorticity thickness is $\delta_{\omega,0} = \delta_\omega(0)$ where $\delta_\omega(t) = \Delta U_0/\left(\partial\langle u_1\rangle/\partial x_2\right)_{\max}$, with the brackets $\langle\rangle$ denoting averaging over homogeneous (x_1, x_3) planes and the velocity difference across the layer is $\Delta U_0 = 2U_0$; the initial mean streamwise velocity has an error-function profile. The specified value of the initial Reynolds number, $\mathrm{Re}_0 = \rho_0 \Delta U_0 \delta_{\omega,0}/\mu$, where ρ_0 is the initial gas density, is used to calculate μ. The thermal conductivity and diffusivity are then computed using this value of μ and specified values of Prandtl and Schmidt numbers of 0.697 (the Lewis number is unity). All thermophysical properties are the same as those employed in the simulations of Miller & Bellan (2000) using air as the carrier gas and decane as the drop liquid.

To promote layer growth, the layer is initially perturbed so as to induce roll-up and pairing. The perturbations, described in Miller & Bellan (1999), follow Moser & Rogers (1991) in specifying spanwise and streamwise vorticity fluctuations, with streamwise and spanwise wavelengths in the x_1 and x_3 directions of $\lambda_1 = 7.29\delta_{\omega,0}$ and $\lambda_3 = 0.6\lambda_1$. For

all the simulations performed herein, $L_1 = 0.2$ m, $L_1 = 4\lambda_1$, $L_2 = 1.1L_1$ and $L_3 = 4\lambda_3$. The relative amplitudes of the forcing perturbations with respect to the circulations are 10% and 2.25% in the spanwise and streamwise directions, respectively. The evolution of the layer comprises two pairings for the four initial spanwise vortices to form a single vortex.

The drops are initially distributed randomly throughout the $x_2 < 0$ domain with specified temperature, velocity, number density and size distribution. Initially, all the drops have the same temperature, $T_{d,0}$, and have the same velocity as the gas phase at their location. The mean number density profile is smoothed near the center-line, $x_2 = 0$, using an error function profile. The drop size distribution is specified through the drop Stokes number $St = \tau_d \Delta U_0/\delta_{\omega,0}$, which is initially given by a Gaussian distribution with mean 3 and standard deviation 0.5. The initial number of drops is determined by the initial mass loading ML_0 (initial ratio of liquid mass to mass of carrier gas in drop-laden part of domain).

The equations are solved numerically using a fourth-order explicit Runge-Kutta temporal integration for time derivatives and eight-order central finite differences with tenth-order filtering for spatial derivatives (Kennedy & Carpenter (1994)). A fourth-order Lagrange interpolation procedure is used to obtain gas-phase variable values at the drop locations.

3. DNS results

The DNS described herein was undertaken to achieve several transitional states that could be further analyzed for *a priori* turbulence modeling. All DNS initial conditions and respective resolutions are listed in Table 1. Four of the cases have initial conditions identical to those of Miller & Bellan (2000); two additional $\mathrm{Re}_0 = 600$ cases, one (SP600)

with no drops and another (TP600a5) with a higher initial mass loading ($ML_0 = 0.5$), have been simulated. As discussed in § 2.1, compared to Miller & Bellan (2000), the gas-phase equations have been expanded to account for enthalpy flux and pressure diffusion effects, with corresponding changes in the boundary conditions. Further, the simulations have been performed for longer nondimensional times compared to those in Miller & Bellan (2000). The rationale behind conducting both TP and SP DNS is that, although the focus is on TP DNS, it is desirable to perform as much gas-phase model development as possible on the SP database. The more of the SP information we can use for TP modeling, the more we can take advantage of the existing body of work pertaining to SP LES modeling and focus our efforts on uniquely drop-related modeling issues. The resolution for the TP cases is the same as that for the SP cases at the same Re_0, and is varied approximately linearly with Re_0. The adequacy of the resolutions is assessed by computing one-dimensional energy spectra at the transitional times with the plots in figure 2 for TP600a2 (streamwise spectra, figure2*a*; spanwise spectra, figure 2*b*) being typical. These plots show that most of the energy is in the large scales (low wave number, k) and that there is no accumulation of energy at high wave numbers.

To understand the characteristics of the mixing layers, we analyze their global and detailed characteristics.

3.1. *Global layer evolution*

The global quantities for the layers are plotted versus the non-dimensional time $t^* = t\Delta U_0/\delta_{\omega,0}$ in figure 3. Among the various quantities available to measure the layer growth, we adopt the momentum thickness δ_m, calculated as

$$\delta_m = \frac{1}{\left(\langle \rho u_1 \rangle_{x_{2,\max}} - \langle \rho u_1 \rangle_{x_{2,\min}}\right)^2} \int_{x_{2,\min}}^{x_{2,\max}} \left[\langle \rho u_1 \rangle_{x_{2,\max}} - \langle \rho u_1 \rangle\right] \left[\langle \rho u_1 \rangle - \langle \rho u_1 \rangle_{x_{2,\min}}\right] dx_2 \tag{3.1}$$

where $x_{2,\max} = L_2/2$ and $x_{2,\min} = -L_2/2$ are the slip wall coordinates. Depicted in figure 3a is $\delta_m/\delta_{\omega,0}$ for all runs listed in Table 1. All layers show consistent growth with two plateaus corresponding to the two pairings, although TP500a5 and TP600a5 show less variations owing to the larger ML_0 which makes the layers more difficult to entrain and thus impedes their growth. All cases have matched values of $\delta_m/\delta_{\omega,0}$ from the beginning of the simulation until roll-up ($t^* \simeq 25$) as the Re_0 or ML_0 specific characteristics are not apparent during roll-up, and then again for t^* between 55 and 70, which is the time between the first pairing ($40 \lesssim t^* \lesssim 50$) and the second pairing ($75 \lesssim t^* \lesssim 90$). In contrast, the layer growth is proportional to ML_0 between roll-up and the end of the first pairing as well as during the second pairing. All runs attain a local maximum for t^* in the range 95 to 105 at which time the value of $\delta_m/\delta_{\omega,0}$ is increasing with ML_0 for the Re_0=600 cases, but increases then decreases with ML_0 for the Re_0=500 cases. This lack of monotonicity for the $\mathrm{Re}_0 = 500$ cases is a manifestation of the initial forcing which has a relatively stronger influence on the smaller Re_0 layer. The transitional times listed in Table 1 correspond to these peaks in $\delta_m/\delta_{\omega,0}$ (these times are rounded to the nearest t^* divisible by 5). Noteworthy, the range of transitional $\delta_m/\delta_{\omega,0}$ values is small (2.49 for SP600 to 2.83 for TP500a2, about 13%).

The global mixing is measured by the product thickness δ_P

$$\delta_P = \int_0^{L_3} \int_{x_{2,\min}}^{x_{2,\max}} \int_0^{L_1} \rho \left[2 \min\left(Y_V, Y_C\right)\right] dx_1 dx_2 dx_3. \tag{3.2}$$

In our simulations, the low vapor mass fraction ($Y_V \lesssim 0.1$) implies that δ_P is essentially twice the mass of vapor in the computational domain (M_V). For the drop laden layers, δ_P is illustrated in figure 3b, while M_V is plotted in figure 3c (non-dimensionalized by the initial mass of gas, $M_{G,0}$) The total liquid mass of the drops (M_L), is plotted in figure 3d which is directly related to the ensemble-averaged drop diameter plotted in figure 3e (discussed below). Both M_V and M_L are seen to depend only on ML_0, with the plots for

TP500a2 and TP600a2 ($ML_0 = 0.2$) and those for TP500a5 and TP600a5 ($ML_0 = 0.5$) overlapping, respectively. Understandably, δ_P increases with ML_0. The initial δ_P growth is larger for $ML_0 = 0.5$, but levels off sooner compared to $ML_0 = 0.2$ as vapor saturation intervenes in the lower stream which stops evaporation, similarly to the situation in Miller & Bellan (1999); however, the ratio of δ_P is much less than that of ML_0 (e.g. 1.2 versus 2.5 at t^*=105). After a period of reduced rate of increase, the δ_P growth for $ML_0 = 0.5$ then increases again which is attributed to the increase in the ensemble-averaged drop temperature (see figure 3f discussed below) that allows increased evaporation. By the end of the simulation, δ_P is still increasing for all layers, meaning that drops are still evaporating (the layer is not saturated). Notably, even at late times, much of the liquid has not evaporated, and the portion of unevaporated liquid depends on ML_0 (e.g. 45% for $ML_0 = 0.2$ leading to $ML = 0.09$, and 74% for $ML_0 = 0.5$ leading to $ML = 0.037$ at t^*=105). This indicates that the interaction of mixing and drop evaporation is very complex so that ML_0 is not quantitatively predictive of the final vapor mass.

Drop-based ensemble averages (for drop-based quantities, $\langle\langle\rangle\rangle$ denotes averaging over all drops), here diameter-squared ($\langle\langle d^2\rangle\rangle$) and temperature ($\langle\langle T_d\rangle\rangle$), illustrated in figures 3*e* and 3*f*, show a dependence only on ML_0, although $\langle\langle T_d\rangle\rangle$ differs slightly between the $ML_0 = 0.2$ cases for $80 \lesssim t^* \lesssim 120$. At the beginning of the simulations, $\langle\langle d^2\rangle\rangle$ decreases at the same rate for all cases this being due to the same $T_{d,0}$ and the same initial gas phase composition, but then the rate of decrease at the higher ML_0 quickly diminishes relative to the lower ML_0 cases which is attributed to the accumulation of vapor in the gas phase (because $\langle\langle T_d\rangle\rangle$ is larger for $ML_0 = 0.5$, and therefore could not be the cause of decreased evaporation rate). Emulating $\langle\langle d^2\rangle\rangle$, the initial variation of $\langle\langle T_d\rangle\rangle$ is the same for all cases, in that it decreases due to the cooling effect of evaporation, but then an oscillatory behavior is observed with the higher ML_0 cases having hotter drops since

the reduced evaporation rate maintains a larger $\langle\langle T_d \rangle\rangle$. As elaborated by Le Clercq & Bellan (2002), the later oscillations in $\langle\langle T_d \rangle\rangle$ are due to the competing effects of heating, which transfers energy from the gas phase, and evaporation, which releases energy into the surrounding gas.

Also depicted in figure 3 are two vorticity measures, the positive spanwise vorticity $\langle\langle \omega_3^+ \rangle\rangle$, (figure 3*g*) and the enstrophy $\langle\langle \omega_i \omega_i \rangle\rangle$, (figure 3*h*), where $\langle\langle\rangle\rangle$ denotes averaging over the entire domain. Initially null, ω_3^+ is a measure of the small-scale activity whereas $\omega_i \omega_i$ is related to stretching and tilting which is an important mechanism for turbulence production. Plotted in figure 3*g*, $\langle\langle \omega_3^+ \rangle\rangle \, \delta_{\omega,0}/\Delta U_0$ grows to an initial peak, at around the time of the first pairing, decreases and then grows again to a higher second peak, after which it declines. The time of the second peak is comparable for SP500 and SP600, being about t^*=80 and approximately corresponding to the time of the second pairing. For the TP cases, the peak is delayed, at about t^*=95 indicating that on a global basis the drops delay vorticity production. The maximum value of $\langle\langle \omega_3^+ \rangle\rangle$ increases with ML_0 at the same Re_0 indicating that the increasing number of drops cause increasing small scale formation effects, and increases with Re_0 at same ML_0, consistent with the well-known Re_0 effect for SP layers; TP600a5 has the largest peak value overall. Finally, $\langle\langle \omega_i \omega_i \rangle\rangle \, (\delta_{\omega,0}/\Delta U_0)^2$ in figure 3*h* shows similar behavior to $\langle\langle \omega_3^+ \rangle\rangle \, \delta_{\omega,0}/\Delta U_0$ in that it peaks sooner for the SP cases than for the TP cases confirming the global indication that the drop presence delays the evolution of vorticity-related attributes, however $\langle\langle \omega \cdot \omega \rangle\rangle \, (\delta_{\omega,0}/\Delta U_0)^2$ peaks sooner than $\langle\langle \omega_3^+ \rangle\rangle \, \delta_{\omega,0}/\Delta U_0$. The TP600a2 curve has distinct behavior compared to the other TP curves in that it exhibits more oscillations; however TP600a5 reaches the maximum enstrophy whereas all other three TP curves attain similar maxima.

In looking at the four global measures depicted in figure 3, the results can be summa-

rized as follows: (1) the variation of $\delta_m/\delta_{\omega,0}$ depends on ML_0 and Re_0 but with no clear trend, (2) δ_P increases with ML_0 but is insensitive to Re_0, and (3) global small-scale generation and enstrophy production increase with ML_0 and with Re_0.

3.2. *Flow visualizations*

Flow visualizations are here scrutinized to detect characteristics that are unavailable in the global measures analyzed above; only the results for the $\mathrm{Re}_0 = 600$ TP cases are shown. To this end, contours of $\omega_3\delta_{\omega,0}/\Delta U_0$ and the drop number density, ρ_n, for TP600a2 and TP600a5 are shown in figure 4, and contours of Y_V and T for the same cases are illustrated in figure 5. The vorticity is qualitatively similar for both cases, with significant numbers of small scale structures distributed throughout the ultimate vortex comprising the mixing region. Notably, the increase in ML_0 decreases the local magnitude of the vorticity, presenting information unavailable from figure 3*g* which showed an increase in $\langle\langle\omega_3^+\rangle\rangle\,\delta_{\omega,0}/\Delta U_0$ with ML_0. Although the ultimate vortex has been somewhat distorted by the small scales, it still retains some coherence at transition. The effect of the vorticity on the drop locations can be seen by comparing figures 4*a* and 4*b* with figures 4*c* and 4*d*, respectively. The low ρ_n regions within and on the lower stream side can be correlated with high vorticity magnitude regions; in contrast, the high ρ_n regions occur at isolated regions within the layer and correlate with low vorticity, either in the free-stream or on the edges of the ultimate vortex. The drop number density is generally smaller for TP600a2, mainly due to the effect of its smaller ML_0 but also due to the disappearance of a larger number of drops that have completely evaporated. An in-depth analysis of the drop organization at transition conducted by Le Clercq & Bellan (2002) and based on ρ_n conditionally averaged on the second invariant of the deformation tensor

for compressible flow,

$$II_u = -\frac{1}{2}\left[(S_{ij}S_{ij} - S_{kk}S_{ll}) - \frac{1}{2}\omega_i\omega_i\right], \tag{3.3}$$

revealed that the drops accumulate most in regions where $II_u \simeq 0$, then in regions where $II_u < 0$ and in the smallest number at locations where $II_u > 0$.

The gas phase temperature, displayed at transition for the TP600a2 and TP600a5 cases in figures 5*a* and 5*b*, exhibits a lower stream where T has decreased from its initial value due to heat transfer to the drops and is close to $T_{d,0}$ (or $\langle\langle T_d \rangle\rangle$, see figure 3*f*), whereas the upper stream is still at $T_{C,0}$. The mixing region is very inhomogeneous and is mostly composed of gas at an intermediate temperature of around 360K, with some colder gas within the layer and warmer layer gas found only adjacent to the warmer stream. The temperature range of TP600a5 (figure 5*b*) is slightly reduced compared to TP600a2 (figure 5*a*), and more of the colder gas has penetrated into the mixing region, consistent with the higher ML_0. The lowest T regions correspond to locations of reduced pressure below the ultimate vortex, and therefore have a lower density than the adjacent lower-stream gas. The Y_V contour plots displayed in figures 5*c* and 5*d* aid in the understanding of the ML_0-related behavior of δ_P (figure 3*b*). Despite the much larger ML_0, the TP600a5 maximum Y_V (about 0.10) is not substantially greater than that of TP600a2 (about 0.09). The gas within the vortex is an inhomogeneous mixture, with the largest Y_V occurring either in the lower stream or at the periphery of the regions of high ρ_n, as shown in figures 4*c* and 4*d*. The highest Y_V regions can be correlated with those of the high ρ_n which occur at isolated locations within the layer. The explanation for this observation is that, although the entire layer is not saturated, by transition the lower stream is close to the saturation Y_V of about 0.09. Therefore, continuing release of vapor can occur only within the mixing region, but of course only where the drops reside.

3.3. *Species-mass and heat flux budgets*

The presence of both T and Y_V gradients in TP flows with evaporating drops directs attention to the form of the vapor mass flux (2.14) and of the heat flux (2.16). For ease of analysis, each flux is split in two terms

$$j_{Vj} = j_{Vj}\left(Y_V\right) + j_{Vj}\left(p\right), \tag{3.4}$$

$$q_j = q_j\left(T\right) + q_j\left(h\right), \tag{3.5}$$

where

$$j_{Vj}\left(Y_V\right) = -\rho D \frac{\partial Y_V}{\partial x_j}, \tag{3.6}$$

$$j_{Vj}\left(p\right) = -Y_C Y_V \left(Y_V + \frac{Y_C m_V}{m_C}\right)\left[\frac{m_C}{m_V} - 1\right]\frac{\rho D}{p}\frac{\partial p}{\partial x_j}, \tag{3.7}$$

$$q_j\left(T\right) = -\lambda \frac{\partial T}{\partial x_j}, \tag{3.8}$$

$$q_j\left(h\right) = \left(h_V - h_C\right) j_{Vj}. \tag{3.9}$$

To evaluate the importance of terms $j_{Vj}\left(p\right)$ and $q_j\left(h\right)$ with respect to $j_{Vj}\left(Y_V\right)$ and $q_j\left(T\right)$, respectively, the DNS database of the TP cases was analyzed at their transitional state; the results for TP600a5 are listed in Table 2 for j_{Vj} and in Table 3 for q_j. Comparisons of two quantities defined at all grid points, $\mathcal{X}\left(x_1, x_2, x_3\right)$ and $\mathcal{Y}\left(x_1, x_2, x_3\right)$, are carried out using a least-squares (LS) fit of $\mathcal{Y} = b\mathcal{X}$ which leads to the slope

$$b = \frac{\langle\langle \mathcal{X}\mathcal{Y} \rangle\rangle}{\langle\langle \mathcal{X}\mathcal{X} \rangle\rangle}. \tag{3.10}$$

From the LS comparison of $j_{Vj}\left(p\right)$ and $j_{Vj}\left(Y_V\right)$ with j_{Vj}, it is obvious that the $j_{Vj}\left(p\right)$ contribution is negligible and that more than 95% is due to $j_{Vj}\left(Y_V\right)$. Clearly, in all directions the root-mean-square (RMS) magnitude of j_{Vj} is close to that of $j_{Vj}\left(Y_V\right)$ and the $j_{Vj}\left(p\right)$ RMS is about one-fifth of that of $j_{Vj}\left(Y_V\right)$. Therefore, it seems legitimate to neglect the pressure contribution in j_{Vj}. In contrast, the dominant contribution to q_j comes from $q_j\left(h\right)$, whose LS slope is three times the magnitude of $q_j\left(T\right)$ and moreover

is of different sign, indicating that the enthalpy term should be definitely be included in the energy equation. Neglecting $q_j(h)$ would lead to the heat transfer vector having an opposite orientation. Also, the RMS of $q_j(h)$ is larger than that of $q_j(T)$, reinforcing the conclusion that $q_j(h)$ must be included in q_j.

4. Derivation of gas-phase LES equations

Following the SP protocol, the LES equations are here derived by spatially filtering the gas-phase DNS equations described in § 2.1, resulting in various unclosed terms that cannot be computed from the filtered flow field. Next, certain simplifying assumptions are assessed that could reduce the complexity of the original LES equations. Finally, the budget of the LES equations is computed to determine if the LES equations can be further simplified by neglecting certain terms. This process identifies those unclosed terms that will require explicit modeling.

4.1. *Filtered gas-phase DNS equations*

The filtering operation is defined as:

$$\bar{\psi}(\vec{x}) = \int_{V_f} \psi(\vec{y})\, G(\vec{x}-\vec{y})\, d\vec{y} \tag{4.1}$$

where G is the filter function, with the property that $\overline{1} = 1$, and V_f is the filtering volume. For finite-difference computations, the filter of choice is a top-hat filter, which is adopted here; then $\bar{\psi}$ is simply the volume-average. The Favre (density-weighted) filtering is defined as $\tilde{\psi} = \overline{\rho\psi}/\bar{\rho}$. It is also assumed that filtering and differentiation commute, which is correct except near boundaries (because the size of the filtering volume decreases as the boundary is approached). The filtered gas-phase equations are

$$\frac{\partial \bar{\rho}}{\partial t} + \frac{\partial(\bar{\rho}\tilde{u}_j)}{\partial x_j} = \bar{S}_I, \tag{4.2}$$

$$\frac{\partial\left(\bar{\rho}\tilde{u}_i\right)}{\partial t}+\frac{\partial\left(\overline{\rho u_i u_j}\right)}{\partial x_j}=-\frac{\partial\bar{p}}{\partial x_i}+\frac{\partial\bar{\sigma}_{ij}}{\partial x_j}+\bar{S}_{II,i}, \tag{4.3}$$

$$\frac{\partial\left(\bar{\rho}\tilde{e}_t\right)}{\partial t}+\frac{\partial\left(\overline{\rho e_t u_j}\right)}{\partial x_j}=-\frac{\partial\left(\overline{p u_j}\right)}{\partial x_j}-\frac{\partial\bar{q}_j}{\partial x_j}+\frac{\partial\left(\overline{\sigma_{ij}u_i}\right)}{\partial x_j}+\bar{S}_{III}, \tag{4.4}$$

$$\frac{\partial\left(\bar{\rho}\tilde{Y}_V\right)}{\partial t}+\frac{\partial\left(\overline{\rho Y_V u_j}\right)}{\partial x_j}=-\frac{\partial\bar{j}_{Vj}}{\partial x_j}+\bar{S}_I. \tag{4.5}$$

From (4.1), the filtered source terms ($\bar{S}=\left\{\bar{S}_I,\bar{S}_{II,i},\bar{S}_{III}\right\}$) are properly interpreted by considering a drop located at $\vec{X}$ within the filtering volume V_f and its contribution within that volume

$$\bar{S}\left(\vec{x}\right)=\int_{V_f}S_d\delta\left(\vec{y}-\vec{X}\right)G\left(\vec{x}-\vec{y}\right)d\vec{y}, \tag{4.6}$$

where $S_d\delta\left(\vec{y}-\vec{X}\right)$ is the point-source contribution from the drop and δ is the delta function. When G is a top-hat filter, the filtered source term is a volume-average over the drops β within the filtering volume

$$\bar{S}\left(\psi_f,Z\right)=\frac{1}{V_f}\sum_{\beta}\left[S_d\right]_{\beta}, \tag{4.7}$$

where S_d was defined in (2.28).

Using the adopted notation of denoting the DNS flow field as ϕ, the filtered flow field can now be denoted as $\bar{\phi}$ and we can formally define functions of $\bar{\phi}$

$$e\left(\bar{\phi}\right),p\left(\bar{\phi}\right),T\left(\bar{\phi}\right),h\left(\bar{\phi}\right),\sigma_{ij}\left(\bar{\phi}\right),j_{Vj}\left(\bar{\phi}\right),q_j\left(\bar{\phi}\right),$$

which have the same functional form as in the DNS but are in general different from their filtered counterparts

$$\tilde{e}=\overline{\rho e\left(\phi\right)}/\bar{\rho},\quad \bar{p}=\overline{p\left(\phi\right)},\quad \bar{T}=\overline{T\left(\phi\right)},\quad \tilde{T}=\overline{\rho T\left(\phi\right)}/\bar{\rho},\quad \tilde{h}=\overline{\rho h\left(\phi\right)}/\bar{\rho}, \tag{4.8}$$

$$\bar{\sigma}_{ij}=\overline{\sigma_{ij}\left(\phi\right)},\quad \bar{j}_{Vj}=\overline{j_{Vj}\left(\phi\right)},\quad \bar{q}_j=\overline{q_j\left(\phi\right)}, \tag{4.9}$$

where $\tilde{h}=\tilde{e}+\bar{p}/\bar{\rho}$. For example, $\tilde{e}=\tilde{e}_t-\widetilde{u_iu_i}/2$, whereas $e\left(\bar{\phi}\right)=\tilde{e}_t-\tilde{u}_i\tilde{u}_i/2$. Moreover, we define SGS fluxes through

$$\tau_{ij}=\widetilde{u_iu_j}-\tilde{u}_i\tilde{u}_j,\quad \zeta_j=\widetilde{hu_j}-\tilde{h}\tilde{u}_j,\quad \eta_j=\widetilde{Y_Vu_j}-\tilde{Y}_V\tilde{u}_j. \tag{4.10}$$

With these notations, the filtered equations become

$$\frac{\partial \bar{\rho}}{\partial t} + \frac{\partial \left(\bar{\rho}\tilde{u}_j\right)}{\partial x_j} = \bar{S}_I, \tag{4.11}$$

$$\begin{aligned}\frac{\partial \left(\bar{\rho}\tilde{u}_i\right)}{\partial t} + \frac{\partial \left(\bar{\rho}\tilde{u}_i\tilde{u}_j\right)}{\partial x_j} &= -\frac{\partial \left[p\left(\bar{\phi}\right)\right]}{\partial x_i} + \frac{\partial \sigma_{ij}\left(\bar{\phi}\right)}{\partial x_j} + \bar{S}_{II,i} - \frac{\partial \left(\bar{\rho}\tau_{ij}\right)}{\partial x_j} \\ &\quad - \frac{\partial}{\partial x_i}\left[\bar{p} - p\left(\bar{\phi}\right)\right] + \frac{\partial}{\partial x_j}\left[\bar{\sigma}_{ij} - \sigma_{ij}\left(\bar{\phi}\right)\right],\end{aligned} \tag{4.12}$$

$$\begin{aligned}\frac{\partial \left(\bar{\rho}\tilde{e}_t\right)}{\partial t} + \frac{\partial \left(\bar{\rho}\tilde{e}_t\tilde{u}_j\right)}{\partial x_j} &= -\frac{\partial \left[p\left(\bar{\phi}\right)\tilde{u}_j\right]}{\partial x_j} - \frac{\partial q_j\left(\bar{\phi}\right)}{\partial x_j} + \frac{\partial \left[\sigma_{ij}\left(\bar{\phi}\right)\tilde{u}_i\right]}{\partial x_j} + \bar{S}_{III} \\ &\quad - \frac{\partial \bar{\rho}\zeta_j}{\partial x_j} - \frac{\partial}{\partial x_j}\left[\tfrac{1}{2}\left(\overline{\rho u_i u_i u_j} - \overline{\rho u_i u_i}\tilde{u}_j\right)\right] \\ &\quad - \frac{\partial}{\partial x_j}\left\{\left[\bar{p} - p\left(\bar{\phi}\right)\right]\tilde{u}_j\right\} - \frac{\partial}{\partial x_j}\left[\bar{q}_j - q_j\left(\bar{\phi}\right)\right] \\ &\quad + \frac{\partial}{\partial x_j}\left[\overline{\sigma_{ij}u_i} - \sigma_{ij}\left(\bar{\phi}\right)\tilde{u}_i\right],\end{aligned} \tag{4.13}$$

$$\frac{\partial \left(\bar{\rho}\tilde{Y}_V\right)}{\partial t} + \frac{\partial \left(\bar{\rho}\tilde{Y}_V\tilde{u}_j\right)}{\partial x_j} = -\frac{\partial j_{Vj}\left(\bar{\phi}\right)}{\partial x_j} + \bar{S}_I - \frac{\partial \left(\bar{\rho}\eta_j\right)}{\partial x_j} - \frac{\partial}{\partial x_j}\left[\bar{j}_{Vj} - j_{Vj}\left(\bar{\phi}\right)\right]. \tag{4.14}$$

Equations (4.11) – (4.14) for $\bar{\phi}$ contain terms that cannot be computed directly from $\bar{\phi}$ and that therefore need to be modeled, namely, (1) the SGS fluxes (τ_{ij}, ζ_j, η_j), (2) the filtered source terms ($\bar{S}_I$, $\bar{S}_{II,i}$, $\bar{S}_{III}$), (3) the velocity triple correlation ($\overline{\rho u_i u_i u_j} - \overline{\rho u_i u_i}\tilde{u}_j$) and (4) the difference terms ($\bar{p} - p\left(\bar{\phi}\right)$, $\bar{\sigma}_{ij} - \sigma_{ij}\left(\bar{\phi}\right)$, $\bar{q}_j - q_j\left(\bar{\phi}\right)$, $\overline{\sigma_{ij}u_i} - \sigma_{ij}\left(\bar{\phi}\right)\tilde{u}_i$, $\bar{j}_{Vj} - j_{Vj}\left(\bar{\phi}\right)$).

4.2. *LES assumptions*

To reduce the modeling requirements, the following assumptions are evaluated *a priori*: for the thermodynamic quantities,

$$\tilde{e} = e\left(\bar{\phi}\right), \quad \overline{T} = T\left(\bar{\phi}\right), \quad \widetilde{T} = T\left(\bar{\phi}\right), \quad \tilde{p} = p\left(\bar{\phi}\right), \quad \tilde{h} = h\left(\bar{\phi}\right); \tag{4.15}$$

for the velocity triple correlation,

$$\tfrac{1}{2}\left(\overline{\rho u_i u_i u_j} - \overline{\rho u_i u_i}\tilde{u}_j\right) = \bar{\rho}\tau_{ij}\tilde{u}_i; \tag{4.16}$$

for the viscous stresses and the velocity-viscous stress correlation,

$$\bar{\sigma}_{ij} = \sigma_{ij}\left(\bar{\phi}\right), \quad \overline{u_i\sigma_{ij}} = \tilde{u}_i\sigma_{ij}\left(\bar{\phi}\right); \tag{4.17}$$

and for the heat and mass fluxes,

$$\bar{j}_{Vj} = j_{Vj}\left(\bar{\phi}\right), \quad \bar{q}_j = q_j\left(\bar{\phi}\right). \tag{4.18}$$

The evaluation of the LES assumptions displayed in (4.15) – (4.18), performed on the filtered DNS databases at the transitional t^*, is summarized in Tables 4–7. For the cubic top-hat filter used here, the filtering volume has sides of length $\bar{\Delta}$. The present results use $\bar{\Delta} = 4\Delta x$, where $\Delta x = \max\left(\Delta x_1, \Delta x_2, \Delta x_3\right)$ (the grid spacing in the three coordinate directions is approximately equal). For each of (4.15) – (4.18), the model (right-hand side of the equations) is linearly correlated to the exact quantity (left-hand side) using a least squares fit. We define the correlation

$$\mathcal{R}\left(\mathcal{X},\mathcal{Y}\right) = \frac{\langle\langle\mathcal{X}\mathcal{Y}\rangle\rangle - \langle\langle\mathcal{X}\rangle\rangle\langle\langle\mathcal{Y}\rangle\rangle}{\sqrt{\left(\langle\langle\mathcal{X}^2\rangle\rangle - \langle\langle\mathcal{X}\rangle\rangle^2\right)}\sqrt{\left(\langle\langle\mathcal{Y}^2\rangle\rangle - \langle\langle\mathcal{Y}\rangle\rangle^2\right)}}, \tag{4.19}$$

where $\mathcal{R}^2$ is the fraction of the variation in $\mathcal{Y}$ due to the variation of $\mathcal{X}$ (Ayyub & McCuen (1997)). If the assumptions were exactly correct, both the slope and the correlation from the least squares fit (computed from (3.10) and (4.19)) of the model to the exact quantity would be unity. From Tables 4–7, it can be seen that the various assumptions are satisfied quite well. For the thermodynamic quantities (Table 4), the slopes range from 1.0003 to 1.0005 (the correlations range from 0.9982 to 1.000). For the velocity triple correlation (Table 5), the slopes range from 1.0148 to 1.056 (the correlations range from 0.972 to 0.994). For the viscous stresses (Table 6), the slopes range from 1.0001 to 1.0008 (the correlations range from 0.9996 to 1.0000). The same table shows $\overline{u_i\sigma_{ij}} = \tilde{u}_i\sigma_{ij}\left(\bar{\phi}\right)$ to be a good assumption with slopes from 0.983 to 1.000 (and correlations of 0.984 to 0.996). Finally the assumptions for the heat and mass fluxes are also valid, based on the slopes

of Table 7. The assumptions for the heat fluxes (that $\bar{q}_j = q_j(\phi)$) appear to hold even better for the TP than for the SP case.

Therefore, the examination of the LES assumptions (4.15) – (4.18) shows that they are justified, and that the appropriate simplifications could be made in (4.12)–(4.14). However, (4.12)–(4.14) contain derivatives of the quantities whose near equality was evaluated in Tables 4–7, and these derivatives are more sensitive to modeling errors than the undifferentiated quantities, prompting us to further consider the budgets of these equations.

4.3. *Budgets of the filtered equations*

The budgets of (4.12)–(4.14) are displayed in Tables 8–12. Results are presented for the filtered flow fields at the transitional t^* indicated on the tables with $\bar{\Delta} = 4\Delta x$. All computations are performed using all grid points i.e. on the DNS (fine) grid, and therefore do not include the discretization error incurred when the differentiations are performed on a presumably coarser LES grid. Although the flow evolution will not be the same in the LES as in the DNS, it seems reasonable to suppose that the unclosed terms of larger magnitude would need to be modeled more accurately.

For the momentum equations (Tables 8–10), the largest contributions are due to the inviscid resolved terms, followed by the SGS stress term. The smallest term (second smallest if $\bar{S}_{II,i} = 0$) is that containing the viscous stress differences. Intermediate between the largest and smallest terms are the pressure difference term, the viscous stress term and the filtered source term (if non-zero); in this order for all cases except TP500a5 and TP600a5. For these two cases, the ordering of the filtered source term compared to the other two terms varies: it is the larger than the other two for the x_1-momentum budget, but in between them for the x_2- and x_3-momentum budgets. For the energy equation (Table 11), the largest term is the resolved inviscid term containing the total energy. The

smallest terms in decreasing order of magnitude are the viscous flux term, the heat flux difference term and the viscous flux difference term. The details of the relative magnitude of the intermediate terms depend on Re_0 and ML_0. For all cases except TP500a5 and TP600a5, the resolved inviscid term containing the pressure is the second largest term with the filtered source term being the third largest term (unless it is null); for TP500a5 and TP600a5, this order is reversed. The next two largest terms are the triple correlation term and the SGS enthalpy flux term, in that order for SP500, SP600 and TP500a2; the SGS enthalpy flux term is the larger term for the other cases. The two remaining terms, the heat flux term and the pressure difference term, are the smallest of the intermediate terms, with the heat flux term being the larger term for the TP cases. For the species equation (Table 12; Y_V is null for the SP cases), the largest contributions are due to the inviscid resolved terms. The next two terms are the SGS species flux term and the filtered source term, with the SGS flux term being the larger one for TP500a2 and TP600a2, but being the smaller one for TP500a5 and TP600a5. The smallest term is the mass flux difference term.

In Tables 8 - 12, the assumptions of (4.15), (4.17) and (4.18) generally lead to the smallest magnitude terms, decisively justifying their neglect. The momentum and species mass source terms are of the same order of magnitude as the resolved viscous stresses and species mass fluxes, respectively, and the energy source term is of the order of the triple correlations, showing that the source terms are of importance in the LES equations; however, the source terms are somewhat smaller than the SGS terms in the momentum equation but of same magnitude as the SGS terms in the energy and species equations. For all the equations, the SGS term tends to be an order of magnitude smaller than the largest, inviscid resolved, term. Thus, from the analysis of the magnitude of various terms, it appears that a successful LES will likely depend mainly on proper resolution

of the filtered flow field, then on good models for the SGS fluxes and finally, for TP flows, on the modeling of source terms. Obviously, to capture the interaction between the drops and the carrier gas, the filtered source terms are needed, and judging from their magnitude, they should be modeled with similar care as the SGS quantities in the species and energy equations.

4.4. *Simplified LES equations*

Upon incorporating the assumptions of (4.15)–(4.18), which have been validated in §4.2 and 4.3, a simpler form of (4.11)–(4.14) is obtained:

$$\frac{\partial \bar{\rho}}{\partial t} + \frac{\partial \left(\bar{\rho}\tilde{u}_j\right)}{\partial x_j} = \bar{S}_I, \tag{4.20}$$

$$\frac{\partial \left(\bar{\rho}\tilde{u}_i\right)}{\partial t} + \frac{\partial \left(\bar{\rho}\tilde{u}_i\tilde{u}_j\right)}{\partial x_j} = -\frac{\partial \left[p\left(\bar{\phi}\right)\right]}{\partial x_i} + \frac{\partial \sigma_{ij}\left(\bar{\phi}\right)}{\partial x_j} + \bar{S}_{II,i} - \frac{\partial \left(\bar{\rho}\tau_{ij}\right)}{\partial x_j}, \tag{4.21}$$

$$\begin{aligned}\frac{\partial \left(\bar{\rho}\tilde{e}_t\right)}{\partial t} + \frac{\partial \left(\bar{\rho}\tilde{e}_t\tilde{u}_j\right)}{\partial x_j} = &-\frac{\partial \left[p\left(\bar{\phi}\right)\tilde{u}_j\right]}{\partial x_j} - \frac{\partial q_j\left(\bar{\phi}\right)}{\partial x_j} + \frac{\partial \left[\sigma_{ij}\left(\bar{\phi}\right)\tilde{u}_i\right]}{\partial x_j} + \bar{S}_{III} \\ &- \frac{\partial \bar{\rho}\zeta_j}{\partial x_j} - \frac{\partial}{\partial x_j}\left[\bar{\rho}\tau_{ij}\tilde{u}_i\right],\end{aligned} \tag{4.22}$$

$$\frac{\partial \left(\bar{\rho}\tilde{Y}_V\right)}{\partial t} + \frac{\partial \left(\bar{\rho}\tilde{Y}_V\tilde{u}_j\right)}{\partial x_j} = -\frac{\partial j_{Vj}\left(\bar{\phi}\right)}{\partial x_j} + \bar{S}_I - \frac{\partial \left(\bar{\rho}\eta_j\right)}{\partial x_j}. \tag{4.23}$$

The modeling effort can now be focused on (1) the SGS fluxes (τ_{ij}, ζ_j, η_j) and (2) the filtered source terms ($\bar{S}_I$, $\bar{S}_{II,i}$, $\bar{S}_{III}$). The *a priori* modeling of these terms will be undertaken in Part II of this investigation.

5. Irreversible entropy production for two-phase flows

A parallel evaluation of the relative magnitude of terms entering the physics of the situation is here obtained by deriving the irreversible entropy production equation for TP flows and analyzing its budget. The irreversible entropy production is the entropy

dissipation, which is of crucial importance in determining the characteristics of turbulent flows.

5.1. *Derivation of entropy equation for two-phase flow with phase change*

According to Hirshfelder *et al.* (1954), the entropy equation is

$$\frac{\partial(\rho s)}{\partial t}+\frac{\partial(\rho s u_j)}{\partial x_j}=-\frac{\partial \Sigma_j}{\partial x_j}+g \tag{5.1}$$

where s is the entropy, Σ_j represents the flux of reversible entropy and g is the rate of irreversible entropy production. In terms of the substantial derivative,

$$\rho\frac{Ds}{Dt}=-\frac{\partial \Sigma_j}{\partial x_j}+g-sS_I. \tag{5.2}$$

From thermodynamics

$$T\frac{Ds}{Dt}=\frac{De}{Dt}+p\frac{D(1/\rho)}{Dt}-\mu_C\frac{DY_C}{Dt}-\mu_V\frac{DY_V}{Dt}, \tag{5.3}$$

where μ_C and μ_V are the chemical potentials of the carrier gas and vapor respectively; $\mu_V=h_V-Ts_V$ where s_V is the entropy of the pure vapor. Mathematical manipulations of (5.3) in conjunction with the conservation equations (2.1)–(2.5) and comparing with (5.2) leads to

$$\Sigma_j=\frac{1}{T}\left(q_j-n_C V_{Cj}\mu_C-n_V V_{Vj}\mu_V\right) \tag{5.4}$$

and

$$\begin{aligned} g=&\frac{1}{T}\left[S_{III}-u_iS_{II,i}+\left(\tfrac{1}{2}u_iu_i-\mu_V\right)S_I\right]\\ &+\frac{\sigma_{ij}}{T}\frac{\partial u_i}{\partial x_j}-\frac{q_j}{T^2}\frac{\partial T}{\partial x_j}-j_{Cj}\frac{\partial}{\partial x_j}\left(\frac{\mu_C}{T}\right)-j_{Vj}\frac{\partial}{\partial x_j}\left(\frac{\mu_V}{T}\right). \end{aligned} \tag{5.5}$$

For an ideal binary mixture of perfect gases (Hirshfelder *et al.* (1954))

$$\frac{\partial}{\partial x_j}\left(\frac{\mu_V}{T}\right)=-\frac{h_V}{T^2}\frac{\partial T}{\partial x_j}+\frac{R_u}{m_V}\frac{1}{p}\frac{\partial p}{\partial x_j}-\frac{R_u}{m_V}\frac{1}{Y_V}\frac{1}{m_C\left(\dfrac{Y_V}{m_V}+\dfrac{Y_C}{m_C}\right)}\frac{\partial Y_C}{\partial x_j}. \tag{5.6}$$

Further manipulations yield the final form of the dissipation as

$$g = g_{III} + g_{II} + g_{I,kine} + g_{I,chpot} + g_{visc} + g_{temp} + g_{mass}, \tag{5.7}$$

where

$$g_{III} = \frac{S_{III}}{T}, \quad g_{II} = -\frac{u_i S_{II,i}}{T}, \quad g_{I,kine} = \frac{\frac{1}{2}u_i u_i S_I}{T}, \quad g_{I,chpot} = -\frac{(h_V - Ts_V)\, S_I}{T}, \tag{5.8}$$

$$g_{visc} = \frac{\mu}{T}\left(2S_{ij}S_{ij} - \frac{2}{3}S_{kk}S_{ll}\right) = \frac{2\mu}{T}\left(S_{ij} - \frac{1}{3}S_{kk}\delta_{ij}\right)\left(S_{ij} - \frac{1}{3}S_{ll}\delta_{ij}\right),$$
$$g_{temp} = \frac{\lambda}{T^2}\frac{\partial T}{\partial x_j}\frac{\partial T}{\partial x_j}, \quad g_{mass} = \frac{R_C R_V}{Y_C Y_V\left(R_V Y_V + R_C Y_C\right)}\frac{j_{V_j} j_{V_j}}{\rho D}. \tag{5.9}$$

The pure vapor entropy, s_V, is calculated for a perfect gas as

$$s_V = \int C_{p,V}\left(T\right)\frac{dT}{T} - \int R_V \frac{dp}{p} \tag{5.10}$$

given a functional form for $C_{p,V}\left(T\right)$, where it is required that s_V be null at 0K (in practice the integration is carried out from 1K due to the logarithmic singularity at $T = 0$). Since $C_{p,V}$ is constant,

$$s_V = s_V^0 + C_{p,V}\ln\left(T/T^0\right) - R_V \ln\left(p/p^0\right), \tag{5.11}$$

where s_V^0 is the reference entropy at the reference temperature T^0 and pressure p^0, obtained from integration or tables, and $C_{p,V} = C_{p,V}\left(T^0\right)$.

Inspection of (5.7) shows that the gas-phase dissipation has several origins. First, the drops are energy, momentum and mass sources with the resulting dissipation embodied in g_{III}, g_{II}, $g_{I,kine}$ and $g_{I,chpot}$. Noteworthy, $g_{I,kine}$ and $g_{I,chpot}$ are entirely due to evaporation, with $g_{I,kine}$ due to the gas-phase kinetic energy of the mass evolving from the drops, whereas $g_{I,chpot}$ is due to its chemical potential. Similar effects are contained in g_{III} and g_{II}, but these terms additionally have non-evaporation contributions from the drag on and the heating of the drops. The terms g_{visc}, g_{temp} and g_{mass} contain the

dissipation due to transport phenomena associated with fluxes and are positive semi-definite.

5.2. *Irreversible entropy production at transitional states*

Before undertaking a detailed analysis of the budget of g (5.7), in figure 6 are presented contour plots of g for TP600a2 (figure 6*a*) and TP600a5 (figure 6*b*) at the transitional times. As in the flow visualizations of figures 4 and 5, both cases show a qualitatively similar aspect; however, the range of TP600a5 dissipation values is more than twice that of TP600a2. Both layers show significant regions of negative dissipation (darkest blue regions), mainly in the lower stream but also in small pockets within the mixing region, although the magnitude of the negative dissipation is less than 10% that of the positive dissipation. Since negative dissipation can arise only from the source-term contributions, this indicates that at those locations turbulence increases due to the presence of the drops. The regions of most intense dissipation are found within the mixing region, and correspond to the high ρ_n regions (see figures 4*c* and 4*d*). From the budget of g, discussed below, it is apparent that this visual correlation between g and ρ_n is due to the g being dominated by the source terms.

The strategy of the dissipation analysis is to first compare results obtained for SP600 and TP600a2 which should reveal the role of the drops, then scrutinize results from TP600a2 and TP600a5 which should elucidate the role of ML_0 and finally consider this information together with results from TP500a2 and TP500a5 to elucidate the influence of Re_0. The data is compared from the perspective of the volume average and RMS budget of (5.7). The information is presented in Table 13 for SP600, Table 14 for TP600a2, Table 15 for TP600a5 and Tables 16 and 17 to compare all four TP cases (some information is repeated from Tables 14 and 15 for easier visual comparison). The terms in all TP tables are arranged according to decreasing RMS of TP500a2 for the DNS (unfiltered)

flow field. All tables contain information at the DNS scale and Tables 13-15 contain additionally information at the LES and SGS scales. The LES (filtered) flow field is obtained by filtering the DNS flow field using the $\bar{\Delta} = 4\Delta x$ box filter and the SGS results are calculated by taking the difference between the DNS-field and LES-field value for each term.

For SP600 (Table 13), g is expectably positive, which means that its effect is to diminish turbulence, and has only two components, g_{visc} and g_{temp}. Due to the compressible nature of the flow, g_{temp} is not null, however it is much smaller than g_{visc} owing to the very small temperature gradients. The dissipation at the LES scale is only about half of the DNS. For the SP calculation, the SGS terms increase the dissipation, both the average and RMS, and this augmentation is comparable in magnitude to the filtered term for the average and much larger than the filtered term for the RMS. The larger magnitude of the SGS RMS compared to that of the filtered terms is expected since the smaller scales are those responsible for the fluctuations associated with turbulence.

For all TP flows and independent of scale (Tables 14 and 15), g is positive in average and considerably larger than its SP equivalent, showing that the global effect of the drops on the flow is to increase dissipation and therefore to decrease turbulence. These results extend into the realm of evaporating drops the information obtained from experimental results with solid particles and no phase change by Hetsroni & Sokolov (1971), Popper *et al.* (1974), Modarress *et al.* (1984), Fleckhaus *et al.* (1987), Tsuji *et al.* (1988), Levy & Lockwood (1981), Hardalupas *et al.* (1989) and Gore & Crowe (1989) which showed that particles smaller than the Kolmogorov length will attenuate turbulence. Owing to the different nature of the present flow fields compared with the solid particle cases, the origin of the leading contributions to g is different. Specifically, for all TP cases the largest term is g_{III}, due to the energy contribution of the drops, and is positive on average.

The second largest term is $g_{I,chpot}$, which is negative on average. Further, an examination of the DNS-field contributions to g_{III} reveals that the $(-\dot{m}_d h_{V,s})$ contribution is the largest followed by that of $(-Q)$, then by $(-F_i v_i)$, and the remaining term with $(-\dot{m}_d v_i v_i/2)$ is the smallest. Therefore the entropy production is overwhelmingly of evaporative and thermodynamic, rather than dynamic, nature. For the flow fields considered, g_{III} dominates $g_{I,chpot}$. However, there may be situations in which $g_{I,chpot}$ will exceed g_{III} in magnitude and, since $g_{I,chpot}$ is negative, lead to evaporating drops enhancing turbulence at the DNS scale, as discussed in conjunction with figures 4*c* and 4*d*. Because $g_{I,chpot}$ is null for solid particles, caution must be exercised in generalizing experimental results obtained with solid particles to the different setting of evaporating drops.

Both the LES-field g_{III} and $g_{I,chpot}$ follow their DNS-field counterparts in being positive and negative, respectively, on average. Notably, the SGS averages have the opposite behavior that is, the average SGS g_{III} is negative and the average SGS $g_{I,chpot}$ is positive, as a consequence of the LES-field dissipation having larger magnitude than that of the DNS. Because g_{III} and $g_{I,chpot}$ represent source terms, this suggests that in LES the correct amount of (global) dissipation cannot be obtained unless the (local) source terms are properly modeled. This conclusion is further borne out by considering the Re_0 and ML_0 behavior of g (see Tables 16 and 17). The DNS-field average g_{III} term increases strongly, but less than proportionally with ML_0 (1.7 for $\mathrm{Re}_0 = 500$ and 2.0 for $\mathrm{Re}_0 = 600$ versus 2.5 increase in ML_0). At the lower ML_0 it increases slightly with Re_0, but at the higher ML_0 it decreases. Behavior similar to that of the average g_{III} is observed for the magnitude of the average $g_{I,chpot}$, as well as for the RMS of both terms. The dominance of g_{III} leads to g mimicking its trends, i.e. being more sensitive to ML_0 than to Re_0 and decreasing/increasing with Re_0 at the lower/higher ML_0. These trends carry over to the LES scale, but not to the SGS scales, where the influence of $g_{I,chpot}$ leads to a

decline in the average g with increasing ML_0. The different behavior of g and its budget, depending on ML_0, inhibit the generalization of low/high ML_0 results, and show the need for robust turbulence modeling that can account for a range of ML_0 by capturing the evolving flow physics.

The largest term not involving source terms is the viscous dissipation term g_{visc}, which is third in order of importance and is about a factor of seven smaller than the two largest terms. The contribution of the SGS g_{visc} terms is larger than that of the filtered terms both for the average and the RMS, thus showing a departure from the SP600 simulation where only the RMS term was larger. For both TP600a2 and TP600a5, at all scales, the g_{visc} contribution is considerably larger than for SP600, showing dissipation due the drop effect on the dynamic field in addition to the source-term dissipation. Following g_{visc}, the next largest term in magnitude is g_{II}. For the TP600a2 DNS field, the magnitude of the average is a factor of 30 smaller than g_{visc} while the RMS is a factor of 3 smaller. At the higher ML_0, g_{II} is closer in magnitude to g_{visc}, with the average being only 11 times smaller than g_{visc} and the RMS being similar in magnitude. For TP600a2 the filtered-field average g_{II} has the same sign as that of the DNS but is about a factor of two larger in magnitude; for TP600a5, the filtered-field g_{II} has the opposite sign and is of same magnitude as that of the DNS. Noteworthy, another ML_0 effect is observed on the DNS field in that for TP600a2 g_{II} is negative on average, whereas for TP600a5 g_{II} is positive on average. This g_{II} behavior is understandable if one considers that $g_{II} \sim [F_i + \dot{m}_d v_i]$ in which on average $F_i > 0$ whereas $\dot{m}_d v_i < 0$. Then it is clear that $g_{II} > 0$ if the drag dominates the mass-change term as for TP600a5, whereas $g_{II} < 0$ if the opposite situation exists as for TP600a2. Finally, the two smallest terms for all TP cases are $g_{I,kine}$ and g_{temp}, the latter being larger at the lower ML_0 but smaller at the higher ML_0 for both Re_0 in the DNS database. The next largest term, g_{mass}, increases with ML_0, indicating

that although the mass fraction range is comparable between TP600a2 and TP600a5 (see figure 5), its gradients are stronger for TP600a5. Similar to g_{visc}, the contribution of the SGS g_{mass} and g_{temp} terms is larger than that of the filtered terms for the RMS, and also for the average g_{temp}. The larger g_{temp} for TP600a2 and TP600a5 compared to SP600 occurs mainly due to gradients arising from the temperature difference between the laden and unladen streams (see figure 5).

Overall, the TP flow fields exhibit positive dissipation, and increased dissipation compared to SP flows, meaning that the effect of the drops is to attenuate turbulence. Although the dissipation due to the viscous stresses is significant, the bulk of the dissipation is associated with the drop evaporation, whether for the DNS solution, the filtered flow field or the small scales. The drop-related dissipation depends on the source terms, which in turn depend on the local flow condition encountered by each drop. Furthermore, this dissipation contains contributions, which may be negative or positive, due to each category (mass, momentum, energy) of source term. The global dissipation, an aggregate over the local contributions, was found not to be readily parametrized through initial global characteristics of the flow field, namely ML_0 and Re_0, for the few values of these parameters that were studied. Routine detailed simulations of ML_0 and Re_0 effects is precluded by the high computational requirements of DNS (see Table 1) and motivates the development of a suitable LES methodology with reduced computational demands. Such a methodology would include careful modeling of local source terms, as it seems unlikely that the proper amount of global dissipation could be achieved without capturing the local flow-drop interactions.

6. Summary and conclusions

We have conducted Direct Numerical Simulations (DNS) of a two-phase temporal mixing layer laden with evaporating drops as a precursor to conducting Large Eddy Simulations (LES) of this flow. The DNS provide a database on which *a priori* analyses of the LES equations can be conducted. The gas-phase was computed in an Eulerian frame using the compressible form of the Navier-Stokes equations along with the conservation of total energy and of carrier gas and vapor masses, whereas the drops were individually tracked in a Lagrangian frame. The gas phase was assumed to obey the perfect gas equation of state. The resolution of the gas phase was adequate for a single-phase flow, with the effect of the drops on the flow being modeled through source terms in the gas-phase equations. Initially, the gas phase consists solely of the carrier gas species and, for two-phase layers, drops are located in the lower stream only and are colder than the gas phase. For the two initial Reynolds numbers (500 and 600) considered, the evolution of single-phase (null mass loading) and two-phase (mass loadings of 0.2 and 0.5) layers was simulated to attain a transitional state for each layer.

For the two-phase layers, the vorticity, temperature and vapor mass fraction fields at transition were qualitatively similar regardless of mass loading. In particular, the temperature of the gas in the initially drop-laden stream diminished to be close and sometimes inferior to the initial drop temperature. Contour plots of the vapor mass fraction at transition showed sensitivity but no strong effect of the initial mass loading for mass loadings of 0.2 or 0.5 in terms of the range or distribution, and the product thickness showed that the layer drops were still evaporating (i.e. the layer was not saturated). Regions of high drop number density occurred in low vorticity locations and exhibited a complex small scale organization documented in detail elsewhere.

In accord with our stated goal of conducting consistent LES, in which both the grid

resolution and the number of tracked drops will be reduced compared to the DNS, we derived the LES equations applicable to two-phase flows with evaporating drops. These LES equations were derived by spatially filtering the DNS equations, leading to unclosed terms that cannot be computed directly from the filtered flow field. By invoking various assumptions, which were validated on the filtered DNS database, and considering the magnitude of the terms in the LES equations at transition, we derived a hierarchy of terms to guide the simplification of the LES equations and reduce the modeling requirements. In particular, we found that many filtered gas-phase quantities are quantitatively close to their counterparts as calculated using the same functional form as in the DNS, but from the filtered flow field. The unclosed terms that were found to be of comparable magnitude at transitional states of two-phase flow and that remain to be modeled are the filtered source terms and the subgrid scale (SGS) fluxes.

The importance of the source terms was further analyzed by deriving the irreversible entropy production (dissipation) equation for two-phase flows with phase change and calculating the dissipation budget at the DNS, LES and subgrid scales. In contrast to single-phase flows where the dissipation is governed by viscous effects, for the two-phase flows studied here the contribution to the dissipation was dominated by terms arising from the drop source term in the gas-phase energy equation which had a positive contribution at the DNS and LES scales, but a negative contribution at the SGS scale. An important, negative DNS and LES scale contribution was identified as coming from the chemical potential of the vapor emanating from the drops, which superseded the contribution from the viscous stresses; at the SGS scale, this terms was found to be positive. At a given initial Reynolds number, the dissipation was found to increase with mass loading, but for a given mass loading, the dissipation decreased with Reynolds number at the lower mass loading but increased with Reynolds number at the higher mass loading; this

behavior showed the need for robust turbulence models that can accommodate a range of mass loadings. Although smaller by an order of magnitude than the viscous dissipation, the average of the dissipation term originating from the momentum source contribution was found at higher mass loadings to be positive at the DNS scale but negative at the LES scale, indicating the importance of the SGS models for portraying the correct physics of the flow since it is possible that at mass loadings larger than those in this study this term may rival the viscous dissipation. The *a priori* modeling of the filtered source terms and the SGS fluxes will constitute the subject of Part II of this investigation.

This work was conducted at the Jet Propulsion Laboratory (JPL) of the California Institute of Technology (Caltech) under the sponsorship of the U.S. Department of Energy (DOE), with Mr. Neil Rossmeissl (DOE Headquarters) and Mr. D. Hooker (DOE Golden Center) serving as contract monitors, under an agreement with the National Aeronautics and Space Administration. Computations were performed on the SGI Origin2000 at the JPL Supercomputing Center.

REFERENCES

AYYUB, B. & MCCUEN, R. 1997 *Probability, Statistics and Reliability for Engineers*. Boca Raton, Florida: CRC Press.

BOIVIN, M., SIMONIN, O. & SQUIRES, K. 1998 Direct numerical simulation of turbulence modulation by particles in isotropic turbulence. *Journal of Fluid Mechanics* **375**, 235–263.

BOIVIN, M., SIMONIN, O. & SQUIRES, K. 2000 On the prediction of gas-solid flows with two-way coupling using large eddy simulation. *Physics of Fluids* **12** (8), 2080–2090.

DEUTSCH, E. & SIMONIN, O. 1991 Large eddy simulation applied to the modelling of particulate transport coefficients in turbulent two-phase flows. In *Eighth Symposium on Turbulent Shear Flows*, pp. 10–1:1–6.

ERLEBACHER, G., HUSSAINI, M., SPEZIALE, C. & ZANG, T. 1992 Toward the large-eddy simulation of compressible turbulent flows. *Journal of Fluid Mechanics* **238**, 155–185.

FLECKHAUS, D., HISHIDA, K. & MAEDA, M. 1987 Effect of laden solid particles on the turbulent flow structure of a round free jet. *Experiments in Fluids* **5**, 323–333.

FUREBY, C. 1996 On subgrid scale modeling in large eddy simulations of compressible fluid flow. *Physics of Fluids A* **8** (5), 1301–1311.

GORE, R. A. & CROWE, C. 1989 Effect of particle size on modulating turbulence intensity. *International Journal of Multiphase Flow* **286**, 229–255.

HARDALUPAS, Y., TAYLOR, A. & WHITELAW, J. 1989 Velocity and particle-flux characteristics of turbulent particle-laden jets. *Proceedings of the Royal Society of London A* **426**, 31–78.

HETSRONI, G. & SOKOLOV, M. 1971 Distribution of mass, velocity, and intensity of turbulence in a two-phase turbulent jet. *Journal of Applied Mechanics, Transactions of the ASME* pp. 315–327.

HIRSHFELDER, J., CURTIS, C. & BIRD, R. 1954 *Molecular Theory of Gases and Liquids*. John Wiley and Sons.

KENNEDY, C. & CARPENTER, M. 1994 Several new numerical methods for compressible shear layer simulations. *Applied Numerical Mathematics* **14**, 397–433.

LE CLERCQ, P. & BELLAN, J. 2002 Direct numerical simulation of a transitional temporal mixing layer laden with multicomponent-fuel evaporating drops using continuous thermodynamics Submitted to Journal of Fluid Mechanics.

LEVY, Y. & LOCKWOOD, F. 1981 Velocity measurements in a particle laden turbulent free jet. *Combustion and Flame* **40**, 333–339.

MARTIN, M., PIOMELLI, U. & CANDLER, G. 2000 Subgrid-scale models for compressible large-eddy simulations. *Theoretical and Computational Fluid Dynamics* **13** (5), 361–376.

MASHAYEK, F. 1998*a* Direct numerical simulations of evaporating droplet dispersion in forced low-Mach-number turbulence. *International Journal of Heat and Mass Transfer* **41** (17), 2601–2617.

MASHAYEK, F. 1998*b* Droplet-turbulence interactions in low-Mach-number homogeneous shear two-phase flows. *Journal of Fluid Mechanics* **367**, 163–203.

MASHAYEK, F. & JABERI, F. 1999 Particle dispersion in forced isotropic low-Mach-number turbulence. *International Journal of Heat and Mass Transfer* **42**, 2823–2836.

MILLER, R. & BELLAN, J. 1999 Direct numerical simulation of a confined three-dimensional gas mixing layer with one evaporating hydrocarbon-droplet laden stream. *Journal of Fluid Mechanics* **384**, 293–338.

MILLER, R. & BELLAN, J. 2000 Direct numerical simulation and subgrid analysis of a transitional droplet laden mixing layer. *Physics of Fluids* **12** (3), 650–671.

MODARRESS, D., TAN, H. & ELGOBASHI, S. 1984 Two-component LDA measurement in a two-phase turbulent jet. *AIAA Journal* **22** (5), 624–630.

MOSER, R. & ROGERS, M. 1991 Mixing transition and the cascade to small scales in a plane mixing layer. *Physics of Fluids A* **3** (5), 1128–1134.

OKONG'O, N. & BELLAN, J. 2000 A priori subgrid analysis of temporal mixing layers with evaporating droplets. *Physics of Fluids* **12** (6), 1573–1591.

POINSOT, T. & LELE, S. 1992 Boundary conditions for direct simulations of compressible viscous flows. *Journal of Computational Physics* **101**, 104–129.

POPPER, J., ABUAF, N. & HETSRONI, G. 1974 Velocity measurements in a two-phase turbulent jet. *International Journal of Multiphase Flow* **1**, 715–726.

RÉVEILLON, J. & VERVISCH, L. 2000 Spray vaporization in nonpremixed turbulent combustion modeling: A single drop model. *Combustion and Flame* **121**, 75–90.

SIMONIN, O., DEUTSCH, E. & BOIVIN, M. 1993 Large eddy simulation and second-moment closure of particle fluctuating motion in two-phase turbulent shear flows. *Turbulent Shear Flows* **9**, 85–115.

TSUJI, Y., MORIKAWA, Y., TANAKA, T., KARIMINE, K. & NISHIDA, S. 1988 Measurement of an axisymmetric jet laden with coarse particles. *International Journal of Multiphase Flow* **14** (5), 565–574.

UIJTTEWAAL, W. & OLIEMANS, R. 1996 Particle dispersion and deposition in direct numerical and large eddy simulations of vertical pipe flows. *Physics of Fluids* **8** (10), 2590–2604.

WANG, Q. & SQUIRES, K. 1996 Large eddy simulations of particle-laden turbulent channel flow. *Physics of Fluids* **8** (5), 1207–1223.

WILLIAMS, F. 1965 *Combustion Theory*. Addison-Wesley.

YAMAMOTO, Y., POTTHOFF, M., TANAKA, T., KAJISHIMA, T. & TSUJI, Y. 2001 Large-eddy simulation of turbulent gas-particle flow in a vertical channel: Effect of considering inter-particle collisions. *Journal of Fluid Mechanics* **442**, 303–334.

Run	Re_0	ML_0	N_d	$N_1 \times N_2 \times N_3$	t^*_{trans}	$\delta_m/\delta_{\omega,0}$ at t^*_{trans}	Re_m at t^*_{trans}	CPU-hours (estimated)
SP500	500	0	0	256×288×160	100	2.580	1290	688
TP500a2	500	0.2	2277222	256×288×160	100	2.827	1414	1336
TP500a5	500	0.5	5693055	256×288×160	105	2.722	1361	2075
SP600	600	0	0	288×320×176	100	2.485	1491	1054
TP600a2	600	0.2	2993630	288×320×176	105	2.627	1576	2252
TP600a5	600	0.5	7484075	288×320×176	105	2.794	1676	3070

Re_0: initial-vorticity-thickness Reynolds number, $\mathrm{Re}_0 = \rho_0 \Delta U_0 \delta_{\omega,0}/\mu$

ML_0: initial mass loading

N_d: initial number of drops

N_1, N_2, N_3: number of grid points in x_1, x_2 and x_3 directions respectively

t^*_{trans}: transition time (dimensionless), $t^* = t\Delta U_0/\delta_{\omega,0}$

Re_m: momentum-thickness Reynolds number, $\mathrm{Re}_m = \rho_0 \Delta U_0 \delta_m/\mu$

CPU hours are estimates on 64 processors of an SGI Origin2000

For all cases: L_1=0.2m, L_2=0.22m, L_3=0.12m , $M_{c,0}$=0.35, $T_{C,0}$=375K, $\delta_{\omega,0}$=6.859×10^{-3}m.

For drop laden cases: $T_{d,0}$=345K, initial St has Gaussian distribution with mean 3, standard deviation 0.5.

TABLE 1. Initial conditions and transition times.

	$j=1$	$j=2$	$j=3$
j_{Vj} (RMS)	1.4857×10^{-2}	1.6396×10^{-2}	1.8450×10^{-2}
$j_{Vj}(Y_V)$ (RMS)	1.4560×10^{-2}	1.6166×10^{-2}	1.8265×10^{-2}
$j_{Vj}(p)$ (RMS)	3.6273×10^{-3}	3.5407×10^{-3}	3.4311×10^{-3}
$j_{Vj}(Y_V)/j_{Vj}$ (LS)	0.9504	0.9628	0.9727
$j_{Vj}(p)/j_{Vj}$ (LS)	0.0496	0.0372	0.0273

RMS=Root-Mean-Square, LS=Least-squares fit slope

TABLE 2. Vapor mass flux (kg $m^{-2}s^{-1}$), TP600a5, t^*=105

	$j=1$	$j=2$	$j=3$
q_j (RMS)	8.7422×10^3	9.6686×10^3	1.0801×10^4
$-\lambda\frac{\partial T}{\partial x_j}$ (RMS)	4.7311×10^3	5.1725×10^3	5.7794×10^3
$(h_V-h_C)j_{Vj}$ (RMS)	1.2875×10^4	1.4208×10^4	1.5992×10^4
$-\lambda\frac{\partial T}{\partial x_j}/q_j$(LS)	-0.4380	-0.4366	-0.4530
$(h_V-h_C)j_{Vj}/\ q_j$(LS)	1.4380	1.4366	1.4530

RMS=Root-Mean-Square, LS=Least-squares fit slope

TABLE 3. Heat flux (J $m^{-2}s^{-1}$), TP600a5, t^*=105

Thermodynamics		Slopes					
Exact	Model	SP500	TP500a2	TP500a5	SP600	TP600a2	TP600a5
$\tilde{e}$	$e\left(\bar{\phi}\right)$	1.0003	1.0005	1.0005	1.0003	1.0004	1.0005
$\overline{T}$	$T\left(\bar{\phi}\right)$	1.0003	1.0005	1.0004	1.0003	1.0003	1.0004
$\widetilde{T}$	$T\left(\bar{\phi}\right)$	1.0003	1.0005	1.0005	1.0003	1.0004	1.0005
$\bar{p}$	$p\left(\bar{\phi}\right)$	1.0003	1.0004	1.0004	1.0003	1.0003	1.0004
$\tilde{h}$	$h\left(\bar{\phi}\right)$	1.0003	1.0005	1.0005	1.0003	1.0003	1.0005

Slope$=\dfrac{\text{Model}}{\text{Exact}}$ from least squares fit

TABLE 4. LES assumptions at transitional times $\bar{\Delta} = 4\Delta x$

Triple velocity correlation		Slopes					
Exact	Model	SP500	TP500a2	TP500a5	SP600	TP600a2	TP600a5
$\frac{1}{2}\left(\overline{\rho u_i u_i u_1} - \overline{\rho u_i u_i}\tilde{u}_1\right)$	$\bar{\rho}\tau_{i1}\tilde{u}_i$	1.0236	1.0263	1.0272	1.0148	1.0199	1.0185
$\frac{1}{2}\left(\overline{\rho u_i u_i u_2} - \overline{\rho u_i u_i}\tilde{u}_2\right)$	$\bar{\rho}\tau_{i2}\tilde{u}_i$	1.0413	1.0520	1.0491	1.0241	1.0375	1.0348
$\frac{1}{2}\left(\overline{\rho u_i u_i u_3} - \overline{\rho u_i u_i}\tilde{u}_3\right)$	$\bar{\rho}\tau_{i3}\tilde{u}_i$	1.0556	1.0526	1.0471	1.0242	1.0382	1.0401

Slope$=\dfrac{\text{Model}}{\text{Exact}}$ from least squares fit

TABLE 5. LES assumptions at transitional times, $\bar{\Delta} = 4\Delta x$, $\tau_{ij} = \widetilde{u_i u_j} - \tilde{u}_i\tilde{u}_j$

Viscous stresses		Slopes					
Exact	Model	SP500	TP500a2	TP500a5	SP600	TP600a2	TP600a5
$\overline{\sigma}_{11}$	$\sigma_{11}\left(\bar{\phi}\right)$	1.0002	1.0003	1.0002	1.0001	1.0002	1.0002
$\overline{\sigma}_{22}$	$\sigma_{22}\left(\bar{\phi}\right)$	1.0003	1.0005	1.0003	1.0002	1.0004	1.0003
$\overline{\sigma}_{33}$	$\sigma_{33}\left(\bar{\phi}\right)$	1.0004	1.0006	1.0004	1.0002	1.0004	1.0004
$\overline{\sigma}_{12}$	$\sigma_{12}\left(\bar{\phi}\right)$	1.0003	1.0004	1.0000	1.0002	1.0002	1.0001
$\overline{\sigma}_{13}$	$\sigma_{13}\left(\bar{\phi}\right)$	1.0003	1.0003	1.0001	1.0002	1.0004	1.0000
$\overline{\sigma}_{23}$	$\sigma_{23}\left(\bar{\phi}\right)$	1.0005	1.0008	1.0004	1.0002	1.0005	1.0003
$\overline{u_i\sigma_{i1}}$	$\tilde{u}_i\sigma_{i1}\left(\bar{\phi}\right)$	0.9953	0.9828	0.9849	0.9930	0.9857	0.9835
$\overline{u_i\sigma_{i2}}$	$\tilde{u}_i\sigma_{i2}\left(\bar{\phi}\right)$	1.0001	0.9905	0.9955	0.9978	0.9949	0.9918
$\overline{u_i\sigma_{i3}}$	$\tilde{u}_i\sigma_{i3}\left(\bar{\phi}\right)$	0.9899	0.9831	0.9881	0.9926	0.9854	0.9843

Slope$=\dfrac{\text{Model}}{\text{Exact}}$ from least squares fit

TABLE 6. LES assumptions at transitional times, $\bar{\Delta} = 4\Delta x$

Fluxes		Slopes					
Exact	Model	SP500	TP500a2	TP500a5	SP600	TP600a2	TP600a5
$\bar{J}_{V1}$	$J_{V1}\left(\bar{\phi}\right)$	–	0.9929	0.9905	–	0.9955	0.9909
$\bar{J}_{V2}$	$J_{V2}\left(\bar{\phi}\right)$	–	0.9925	0.9914	–	0.9949	0.9910
$\bar{J}_{V3}$	$J_{V3}\left(\bar{\phi}\right)$	–	0.9941	0.9922	–	0.9962	0.9911
$\bar{q}_1$	$q_1\left(\bar{\phi}\right)$	1.0353	1.0011	0.9980	1.0324	1.0005	0.9987
$\bar{q}_2$	$q_2\left(\bar{\phi}\right)$	1.0766	1.0007	0.9981	1.0521	0.9999	0.9994
$\bar{q}_3$	$q_3\left(\bar{\phi}\right)$	1.0756	1.0025	0.9994	1.0598	1.0012	0.9991

Slope$=\dfrac{\text{Model}}{\text{Exact}}$ from least squares fit

TABLE 7. LES assumptions at transitional times, $\bar{\Delta} = 4\Delta x$

x_1 Momentum	SP500	TP500a2	TP500a5	SP600	TP600a2	TP600a5
t^*	100	100	105	100	105	105
$\frac{\partial}{\partial x_j}\left(\bar{\rho}\tilde{u}_1\tilde{u}_j\right)$	3.0367×10^5	3.9239×10^5	3.5669×10^5	3.0189×10^5	3.5057×10^5	4.0678×10^5
$\frac{\partial}{\partial x_1}\left[p\left(\bar{\phi}\right)\right]$	2.0147×10^5	2.5665×10^5	2.1671×10^5	1.8383×10^5	2.0398×10^5	2.3919×10^5
$\frac{\partial}{\partial x_j}\left[\sigma_{1j}\left(\bar{\phi}\right)\right]$	1.0084×10^4	1.3785×10^4	1.3762×10^4	9.6983×10^3	1.1822×10^4	1.4236×10^4
$\bar{S}_{II,1}$	0	1.1374×10^4	2.8232×10^4	0	1.0295×10^4	3.1087×10^4
$\frac{\partial}{\partial x_j}\left(\bar{\rho}\tau_{1j}\right)$	3.1846×10^4	5.8967×10^4	5.6381×10^4	3.1105×10^4	4.8058×10^4	6.5798×10^4
$\frac{\partial}{\partial x_1}\left[\bar{p}-p\left(\bar{\phi}\right)\right]$	1.5788×10^4	2.6245×10^4	2.2962×10^4	1.4540×10^4	2.0341×10^4	2.6780×10^4
$\frac{\partial}{\partial x_j}\left[\bar{\sigma}_{1j}-\sigma_{1j}\left(\bar{\phi}\right)\right]$	1.0576×10^2	3.7938×10^2	3.6318×10^2	7.8458×10^1	2.6273×10^2	3.6048×10^2

TABLE 8. Magnitude (RMS) of terms in LES equations, $\bar{\Delta}=4\Delta x$. Units are Nm^{-3}.

x_2 Momentum	SP500	TP500a2	TP500a5	SP600	TP600a2	TP600a5
t^*	100	100	105	100	105	105
$\frac{\partial}{\partial x_j}\left(\bar{\rho}\tilde{u}_2\tilde{u}_j\right)$	3.2687×10^5	4.6623×10^5	4.2759×10^5	3.3349×10^5	4.1267×10^5	4.8311×10^5
$\frac{\partial}{\partial x_2}\left[p\left(\bar{\phi}\right)\right]$	1.6314×10^5	2.5560×10^5	2.0143×10^5	1.3690×10^5	1.8192×10^5	2.2048×10^5
$\frac{\partial}{\partial x_j}\left[\sigma_{2j}\left(\bar{\phi}\right)\right]$	9.0552×10^3	1.2447×10^4	1.1861×10^4	8.5216×10^3	1.0611×10^4	1.2292×10^4
$\bar{S}_{II,2}$	0	9.0370×10^3	2.2930×10^4	0	6.9249×10^3	2.5463×10^4
$\frac{\partial}{\partial x_j}\left(\bar{\rho}\tau_{2j}\right)$	3.3506×10^4	6.3069×10^4	5.6244×10^4	3.0800×10^4	4.8879×10^4	6.4715×10^4
$\frac{\partial}{\partial x_2}\left[\bar{p}-p\left(\bar{\phi}\right)\right]$	1.9788×10^4	2.9582×10^4	2.6395×10^4	1.7619×10^4	2.3147×10^4	3.0268×10^4
$\frac{\partial}{\partial x_j}\left[\bar{\sigma}_{2j}-\sigma_{2j}\left(\bar{\phi}\right)\right]$	7.8404×10^2	9.2795×10^2	6.6760×10^2	6.5071×10^2	4.4696×10^2	6.6685×10^2

TABLE 9. Magnitude (RMS) of terms in LES equations, $\bar{\Delta}=4\Delta x$. Units are Nm^{-3}.

x_3 Momentum	SP500	TP500a2	TP500a5	SP600	TP600a2	TP600a5
t^*	100	100	105	100	105	105
$\frac{\partial}{\partial x_j}\left(\bar{\rho}\tilde{u}_3\tilde{u}_j\right)$	3.1593×10^5	4.2510×10^5	4.0625×10^5	3.1457×10^5	4.0645×10^5	4.6594×10^5
$\frac{\partial}{\partial x_3}\left[p\left(\bar{\phi}\right)\right]$	1.4502×10^5	2.1117×10^5	1.8436×10^5	1.0530×10^5	1.5672×10^5	2.0626×10^5
$\frac{\partial}{\partial x_j}\left[\sigma_{3j}\left(\bar{\phi}\right)\right]$	7.919×10^3	1.0641×10^4	1.0361×10^4	7.5605×10^3	9.2435×10^3	1.0935×10^4
$\tilde{S}_{II,3}$	0	6.9828×10^3	1.9849×10^4	0	5.5845×10^3	2.1513×10^4
$\frac{\partial}{\partial x_j}\left(\bar{\rho}\tau_{3j}\right)$	3.4452×10^4	6.1074×10^4	5.3654×10^4	3.1263×10^4	4.8471×10^4	6.4076×10^4
$\frac{\partial}{\partial x_3}\left[\bar{p}-p\left(\bar{\phi}\right)\right]$	2.0078×10^4	3.3437×10^4	2.9066×10^4	1.8425×10^4	2.4512×10^4	3.3008×10^4
$\frac{\partial}{\partial x_j}\left[\bar{\sigma}_{3j}-\sigma_{3j}\left(\bar{\phi}\right)\right]$	1.5576×10^3	1.7452×10^3	1.2392×10^3	1.2952×10^3	7.9873×10^2	1.2374×10^3

TABLE 10. Magnitude (RMS) of terms in LES equations, $\bar{\Delta}=4\Delta x$. Units are Nm^{-3}.

Energy	SP500	TP500a2	TP500a5	SP600	TP600a2	TP600a5
t^*	100	100	105	100	105	105
$\frac{\partial}{\partial x_j}\left(\bar{\rho}\tilde{e}_t\tilde{u}_j\right)$	4.6200×10^7	2.2466×10^8	2.5341×10^8	4.4946×10^7	2.2398×10^8	2.7598×10^8
$\frac{\partial}{\partial x_j}\left[p\left(\bar{\phi}\right)\tilde{u}_j\right]$	1.6125×10^7	2.4558×10^7	2.0164×10^7	1.5226×10^7	1.7014×10^7	2.3191×10^7
$\frac{\partial}{\partial x_j}\left[q_j\left(\bar{\phi}\right)\right]$	1.6647×10^6	6.3360×10^6	7.6312×10^6	1.4881×10^6	5.6522×10^6	7.5173×10^6
$\frac{\partial}{\partial x_j}\left[\sigma_{ij}\left(\bar{\phi}\right)\tilde{u}_i\right]$	1.1390×10^6	1.5858×10^6	1.4413×10^6	1.0697×10^6	1.2488×10^6	1.5246×10^6
$\tilde{S}_{III}$	0	1.8345×10^7	2.8614×10^7	0	1.5530×10^7	3.0344×10^7
$\frac{\partial}{\partial x_j}\left(\bar{\rho}\zeta_j\right)$	2.4296×10^6	1.2689×10^7	1.4941×10^7	2.1851×10^6	1.1215×10^7	1.5805×10^7
$\frac{\partial}{\partial x_j}\left(\overline{\rho e_k u_j}-\overline{\rho e_k}\tilde{u}_j\right)$	7.0306×10^6	1.3260×10^7	1.1304×10^7	6.6728×10^6	9.8611×10^6	1.3999×10^7
$\frac{\partial}{\partial x_j}\left\{\left[\bar{p}-p\left(\bar{\phi}\right)\right]\tilde{u}_j\right\}$	1.6165×10^6	2.7917×10^6	2.2607×10^6	1.5788×10^6	2.0174×10^6	2.7330×10^6
$\frac{\partial}{\partial x_j}\left[\bar{q}_j-q_j\left(\bar{\phi}\right)\right]$	7.2435×10^5	6.8468×10^5	4.7080×10^5	6.2555×10^5	4.5018×10^5	4.8847×10^5
$\frac{\partial}{\partial x_j}\left[\overline{\sigma_{ij}u_i}-\sigma_{ij}\left(\bar{\phi}\right)\tilde{u}_i\right]$	2.4423×10^5	4.5338×10^5	4.0946×10^5	2.1616×10^5	3.1954×10^5	4.3738×10^5

TABLE 11. Magnitude (RMS) of terms in LES equations, $\bar{\Delta}=4\Delta x$. Units are Jm^{-3}.

Species	TP500a2	TP500a5	TP600a2	TP600a5
t^*	100	105	105	105
$\frac{\partial}{\partial x_j}\left(\bar{\rho}\tilde{Y}_V\tilde{u}_j\right)$	1.8948×10^2	2.2142×10^2	1.9214×10^2	2.3922×10^2
$\frac{\partial}{\partial x_j}\left[j_{Vj}\left(\bar{\phi}\right)\right]$	1.1557×10^1	1.2799×10^1	1.0125×10^1	1.2683×10^1
$\bar{S}_I$	2.0684×10^1	3.2703×10^1	1.7522×10^1	3.4552×10^1
$\frac{\partial}{\partial x_j}\left(\bar{\rho}\eta_j\right)$	2.4166×10^1	2.6041×10^1	2.1016×10^1	2.7823×10^1
$\frac{\partial}{\partial x_j}\left[\overline{j_{Vj}}-j_{Vj}\left(\bar{\phi}\right)\right]$	8.0931×10^{-1}	8.8136×10^{-1}	5.9755×10^{-1}	9.2112×10^{-1}

TABLE 12. Magnitude (RMS) of terms in LES equations, $\bar{\Delta} = 4\Delta x$. Units are kg $s^{-1}m^{-3}$.

	Unfiltered		Filtered		Difference (SGS)	
Term	Average	RMS	Average	RMS	Average	RMS
g_{visc}	1640	3914	848	1720	791	2474
g_{temp}	13	36	6	13	7	27
g	1652	3932	854	1726	798	2484

TABLE 13. Entropy production of unfiltered and filtered flow fields, SP600 at $t^* = 100, \bar{\Delta} = 4\Delta x$. Units are $Wm^{-3}K^{-1}$.

	Unfiltered		Filtered		Difference (SGS)	
Term	Average	RMS	Average	RMS	Average	RMS
g_{III}	13819	40010	15498	49319	-1680	14180
$g_{I,chpot}$	-8014	24935	-9012	30571	998	8590
g_{visc}	2658	6372	1264	2526	1394	4319
g_{II}	-89	2405	-237	2752	148	1030
g_{mass}	222	1302	109	361	113	1144
g_{temp}	122	401	49	128	73	308
$g_{I,kine}$	57	266	63	306	-6	86
g	8775	19177	7735	20205	1040	6810

TABLE 14. Entropy production of unfiltered and filtered flow fields, TP600a2 at $t^* = 105, \bar{\Delta} = 4\Delta x$. Units are $\mathrm{Wm^{-3}K^{-1}}$.

	Unfiltered		Filtered		Difference (SGS)	
Term	Average	RMS	Average	RMS	Average	RMS
g_{III}	27659	79084	32478	98281	-4818	31057
$g_{I,chpot}$	-15768	49784	-18431	60709	2663	18129
g_{visc}	3764	8929	1721	3357	2043	6253
g_{II}	343	8260	-292	9797	635	4186
g_{mass}	304	3338	155	517	149	3224
g_{temp}	157	498	65	177	92	369
$g_{I,kine}$	136	575	152	646	-16	190
g	16594	36370	15874	40663	747	13527

TABLE 15. Entropy production of unfiltered and filtered flow fields, TP600a5 at $t^* = 105, \bar{\Delta} = 4\Delta x$. Units are $\mathrm{Wm^{-3}K^{-1}}$.

Term	TP500a2 $t^* = 100$	TP500a5 $t^* = 105$	TP600a2 $t^* = 105$	TP600a5 $t^* = 105$
g_{III}	15996	26765	13819	27659
$g_{I,chpot}$	-9353	-15119	-8014	-15768
g_{visc}	3718	3469	2658	3764
g_{II}	-111	303	-89	343
g_{mass}	289	317	222	304
g_{temp}	169	153	122	157
$g_{I,kine}$	80	128	57	136
g	10789	16017	8775	16594

TABLE 16. Average entropy production of transitional flow fields. Units are $\mathrm{Wm^{-3}K^{-1}}$.

Term	TP500a2 $t^* = 100$	TP500a5 $t^* = 105$	TP600a2 $t^* = 105$	TP600a5 $t^* = 105$
g_{III}	47358	74878	40010	79084
$g_{I,chpot}$	29332	47339	24935	49784
g_{visc}	9003	8039	6372	8929
g_{II}	3181	7392	2405	8260
g_{mass}	1157	1323	1302	3338
g_{temp}	543	512	401	498
$g_{I,kine}$	342	536	266	575
g	23513	34440	19177	36370

TABLE 17. RMS entropy production of transitional flow fields. Units are $\mathrm{Wm^{-3}K^{-1}}$.

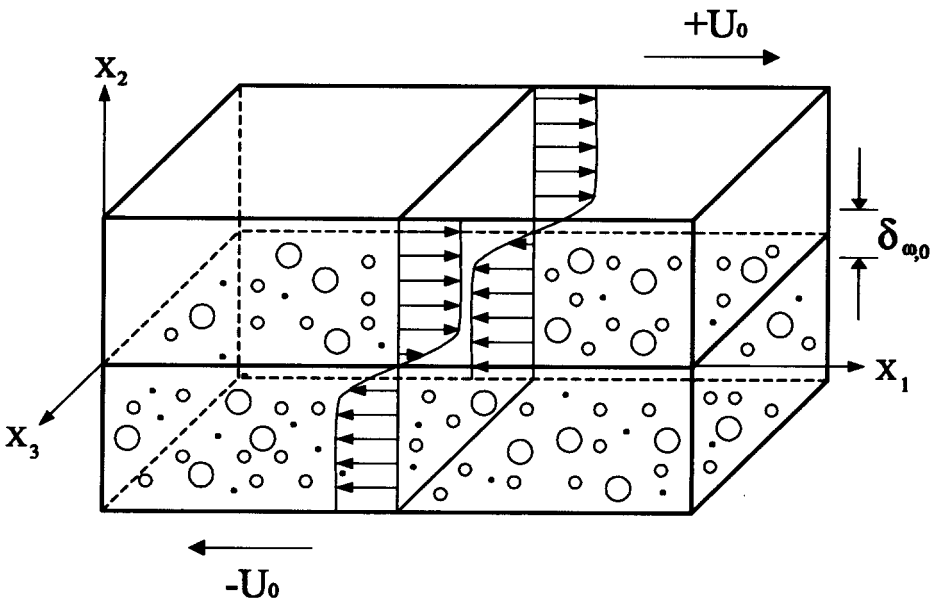

FIGURE 1. Mixing layer configuration

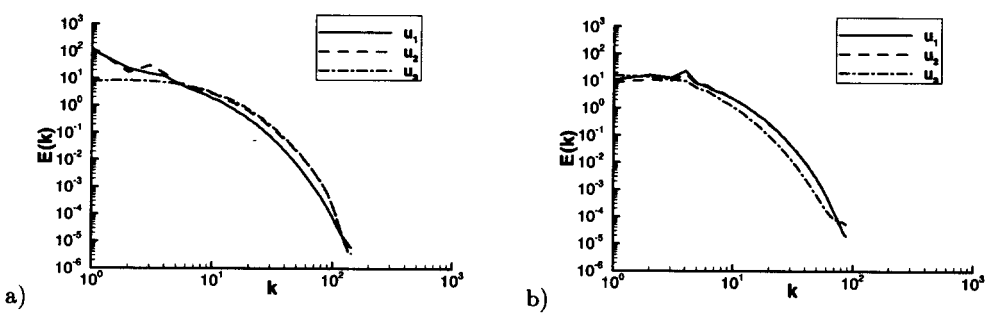

FIGURE 2. One-dimensional energy spectra, TP600a2, t^*=105: a) streamwise b) spanwise

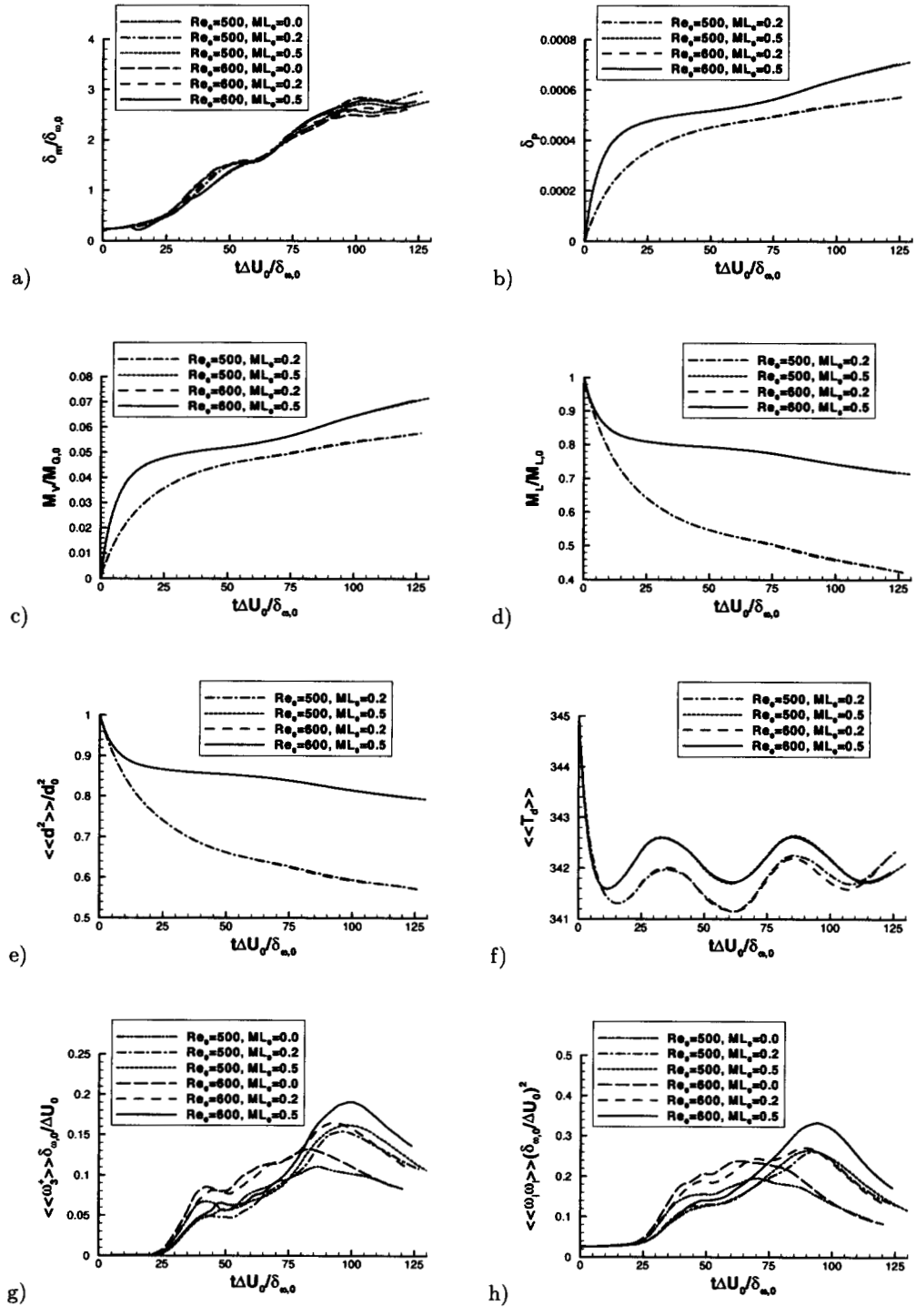

FIGURE 3. Time evolution of global quantities: a) momentum thickness, b) product thickness (kg), c) mass of vapor, d) mass of liquid, e) average drop diameter-squared, f) average drop temperature (K), g) average positive spanwise vorticity and h) enstrophy; (a,g,h) for all layers, (b–f) for drop-laden layers.

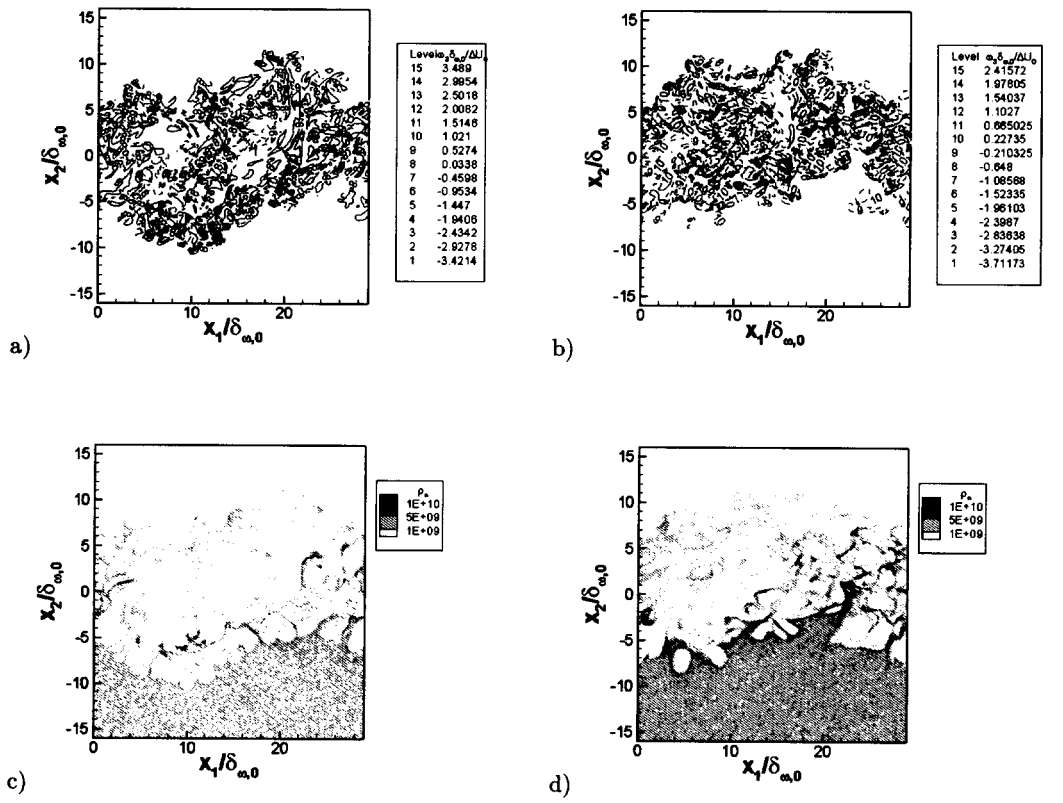

FIGURE 4. (a,b) Spanwise vorticity and (c,d) drop number density (m^{-3}) for (a,c) TP600a2 at t^*=105 and (b,d) TP600a5 at t^*=105, in the between-the-braid plane (x_3/L_3=0.5). Dashed lines are used for negative values of vorticity.

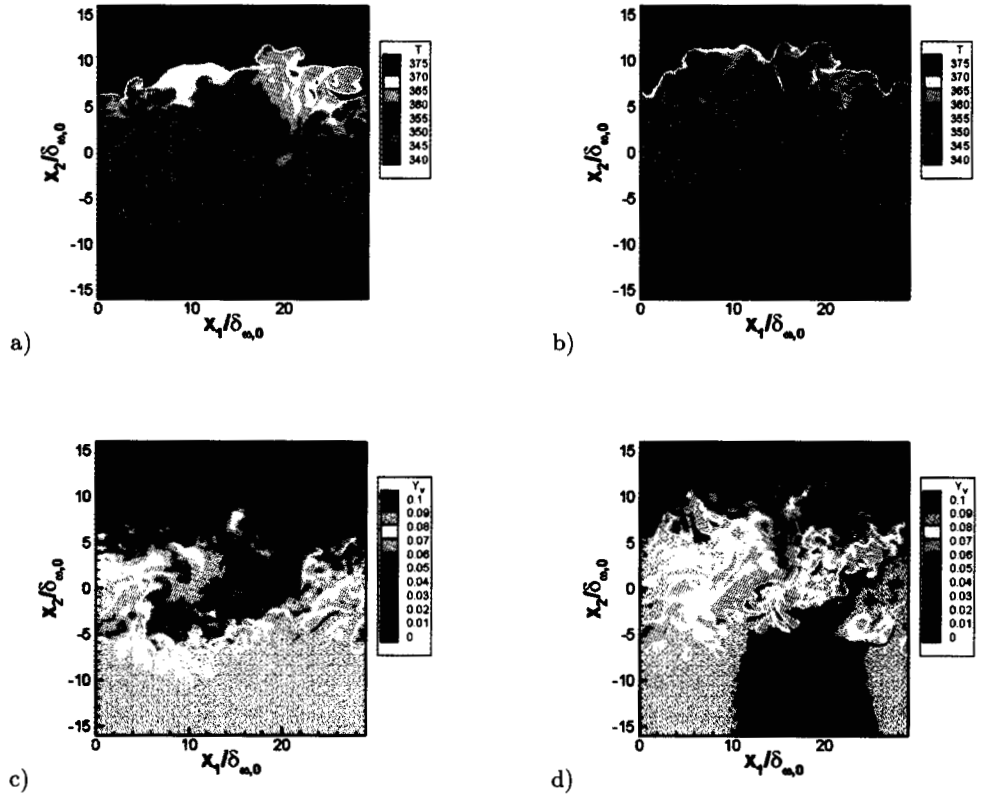

FIGURE 5. (a,b) Temperature (K) and (c,d) vapor mass fraction for (a,c) TP600a2 at t^*=105 and (b,d) TP600a5 at t^*=105, in the between-the-braid plane.

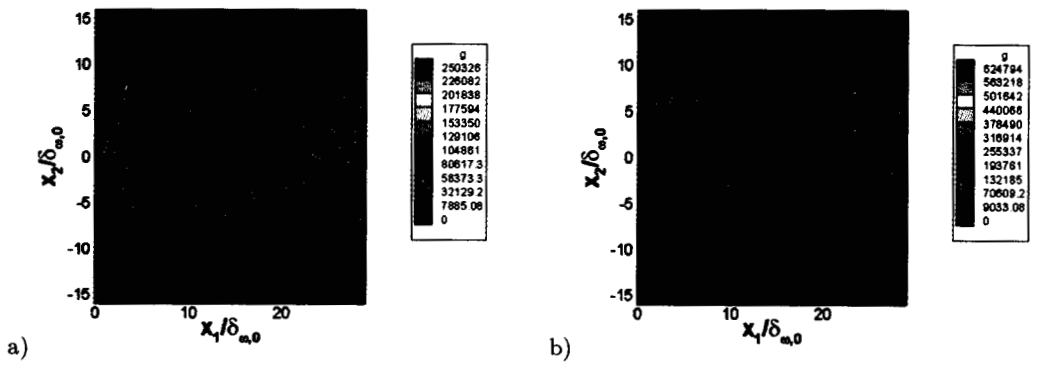

FIGURE 6. Irreversible entropy production ($\mathrm{Wm^{-3}K^{-1}}$) for a) TP600a2 at t^*=105 and b) TP600a5 at t^*=105, in the between-the-braid plane.